JOURNAL OF GEOPHYSICAL RESEARCH, VOL. 111, E12004, doi:10.1029/2006JE002735, 2006

High-resolution thermal inertia derived from the Thermal Emission Imaging System (THEMIS): Thermal model and applications

Robin L. Fergason,[1] Philip R. Christensen,[1] and Hugh H. Kieffer[2]

Received 21 April 2006; revised 10 July 2006; accepted 20 July 2006; published 8 December 2006.

[1] Thermal inertia values at 100 m per pixel are determined using nighttime temperature data from the Thermal Emission Imaging System (THEMIS) on the Mars Odyssey spacecraft, producing the highest-resolution thermal inertia data set to date. THEMIS thermal inertia values have an overall accuracy of ~20%, a precision of 10–15%, and are consistent with both Thermal Emission Spectrometer orbital and Miniature Thermal Emission Spectrometer surface thermal inertia values. This data set enables the improved quantification of fine-scale surface details observed in high-resolution visible images. In the Tharsis region, surface textures and crater rims observed in visible images have no corresponding variation in the THEMIS thermal inertia images, indicating that the dust mantle is pervasive at THEMIS scales and is a minimum of a few centimeters and up to 1–2 m thick. The thermal inertia of bed form material indicates particle diameters expected for aeolian sediments, and these materials are likely currently saltating. Variations in the thermal inertia within interior layered deposits in Hebes Chasma can be distinguished, and the thermal inertia is too low to be consistent with bedrock or a lava flow. Thus a secondary emplacement of volcanic material or a volcanic ash deposit is a more likely method of formation. Higher-resolution THEMIS thermal inertia enables the identification of exposed bedrock on the Martian surface. In Nili Patera and Ares Vallis, bedrock material corresponds to distinct compositional and morphologic surfaces, indicating that a specific unit is exposed and is likely currently being kept free of unconsolidated material by aeolian processes.

Citation: Fergason, R. L., P. R. Christensen, and H. H. Kieffer (2006), High-resolution thermal inertia derived from the Thermal Emission Imaging System (THEMIS): Thermal model and applications, *J. Geophys. Res.*, *111*, E12004, doi:10.1029/2006JE002735.

1. Introduction

[2] The Thermal Emission Imaging System (THEMIS) on the Mars Odyssey spacecraft [*Christensen et al.*, 2004] acquires daytime and nighttime infrared images at 100 m per pixel, and provides thermophysical information at the highest spatial resolution to date. THEMIS nighttime temperature images are used to derive thermal inertia values that quantify the physical properties and average particle sizes of surface textures and morphologies observed in high-resolution Mars Orbiter Camera (MOC) [*Malin et al.*, 1992; *Malin and Edget*, 2001] and THEMIS visible images. This data set allows the comparison between similar features, such as intracrater deposits, bedrock exposures, or layered morphologies, observed in different localities on the planet and in images acquired at different local times or seasons. Understanding the processes that created surfaces at local scales allows these observations to be extrapolated to regional and global scales.

[3] Thermal inertia is a valuable aid to understanding the surficial geology and recent processes that are potentially still active today. To demonstrate the insight into Martian geologic processes provided by this high-resolution data set, we will: (1) describe an algorithm that calculates thermal inertia values from THEMIS nighttime temperature data; (2) discuss the uncertainties in this method and how these uncertainties propagate into errors in thermal inertia calculations; (3) compare THEMIS-derived thermal inertia values to previous data sets, including orbital values from the Thermal Emission Spectrometer (TES) onboard the Mars Global Surveyor (MGS) [*Christensen et al.*, 1992, 2001] and surface data from the Mars Exploration Rover (MER) Miniature Thermal Emission Spectrometer (Mini-TES) [*Christensen et al.*, 2003b] experiments; and (4) investigate examples of dusty surfaces, bed form morphologies, interior layered deposits, and exposed bedrock.

1.1. THEMIS Instrument Description

[4] The Mars Odyssey spacecraft is in a near-polar sun synchronous orbit with a drifting equator-crossing local time, ranging from 3 AM and 3 PM to 6 AM and 6 PM. The orbit has remained between 5 and 6 AM/PM since July 2003, and will remain in this orbit until the end of the first extended mission (August 2006). This orbit is good for observing nighttime temperatures at the mid to equatorial

[1] School of Earth and Space Exploration, Mars Space Flight Facility, Arizona State University, Tempe, Arizona, USA.
[2] Celestial Reasonings, Carson City, Nevada, USA.

0148-0227/06/2006JE002735$09.00

latitudes, provided the surface temperature is not below CO_2 condensation temperatures (about 148 K), because at this time the effects of albedo and slopes on surface temperature have largely dissipated while effects due to the physical properties of the surface remain [*Kieffer et al.*, 1973, 1977; *Christensen et al.*, 2001].

[5] THEMIS infrared data are acquired using a multispectral microbolometer array with 320 cross-track pixels and 240 down-track pixels. It has an instantaneous field of view (IFOV) of ~100 m per pixel and an image width of ~32 km. Spectral differentiation in the infrared is achieved with 10 narrowband stripe filters that produce ~1-μm-wide bands at nine separate wavelengths from 6.78 to 14.88 μm. These bands include nine surface-sensing wavelengths (bands 1–9), and one atmospheric wavelength (band 10) [*Christensen et al.*, 2004]. Two filters (bands 1 and 2) cover the same wavelength range (centered at 6.78 μm) to improve the signal to noise in that spectral region. Standard THEMIS data processing consists of decompression, radiometric calibration, and systematic noise removal. Images can also be geometrically corrected, and multiple images can then be mosaiced together [*Christensen et al.*, 2004].

1.2. Thermal Inertia Background

[6] Thermal inertia represents the resistance to change in temperature of the upper few centimeters of the surface throughout the day, and is independent of local time, latitude, and season. It is defined as $I = (k\rho c)^{1/2}$, where k is the thermal conductivity, ρ is the bulk density of the surface material, and c is the specific heat (units are J m^{-2} K^{-1} $s^{-1/2}$ throughout this work; a scale factor of 41.86 converts to Viking-era 10^{-3} cal cm^{-2} K^{-1} $s^{-1/2}$ units). Under Martian atmospheric conditions, the density and specific heat of geologic materials vary by factors of ~3, whereas the conductivity varies by 3–4 orders of magnitude and therefore has the strongest influence on the thermal inertia [e.g., *Wechsler and Glaser*, 1965; *Neugebauer et al.*, 1971; *Wechsler et al.*, 1972; *Presley and Christensen*, 1997a]. The bulk conductivity of a material is a function of the solid, radiative, and gas conductivity. At Martian surface temperatures, radiative conductivity is a small contribution compared to the solid and gas conductivity [*Wechsler et al.*, 1972]. The solid and gas conductivity is largely controlled by the relationship between the particle size and the pore size relative to the mean-free-path of a gas (~5 μm at Martian pressures). When the pore size is comparable in size or smaller than the gas mean free path (relatively small grains), gas molecule collisions with the grains become less frequent, resulting in an inefficient transfer of heat. Decreasing the particle size also increases the number of grain-to-grain contacts per unit length, and further decreases conduction [*Jakosky*, 1986; *Presley and Christensen*, 1997b]. As a result, the thermal inertia is strongly controlled by particle size, and can be related to an effective particle size, assuming unconsolidated, homogeneous spheres to a depth of ~5 thermal skin depths [*Kieffer et al.*, 1973; *Presley and Christensen*, 1997b].

[7] Laboratory-derived relationships between particle size and conductivity have been established [e.g., *Woodside and Messmer*, 1961; *Wechsler and Glaser*, 1965; *Fountain and West*, 1970; *Presley and Christensen*, 1997b, 1997c] and are used to infer an effective particle size of the surface from thermal inertia values. Fine particles have a lower thermal inertia, whereas higher thermal inertia surfaces are composed of sand, duricrust, rock fragments, or a combination of these materials. Several features can complicate the modeling of thermal inertia and make interpreting thermal inertia results challenging. These include, but are not limited to, the mixing of different particle sizes, the presence of duricrust, subsurface layering, sub-pixel-scale slopes, dust in the atmosphere, and water-ice clouds. The interpretation of thermal inertia as an effective particle size is less ambiguous if the thermal inertia is low (dust) or very high (bedrock), but many equally plausible scenarios can result in a particle size described by the moderate thermal inertia of a surface. Thus thermal inertia does not provide a unique characterization of the surface physical characteristics [*Christensen*, 1982], but does provide significant insight into the physical nature of the surface and is uniquely related to an effective particle size [e.g., *Kieffer et al.*, 1973; *Fergason et al.*, 2006].

1.3. Previous Work

[8] Thermophysical data of Mars were collected by Mariners 6, 7, and 9 [*Neugebauer et al.*, 1971; *Kieffer et al.*, 1973], and the first thermal inertia maps were made using temperatures from the Infrared Thermal Mapper (IRTM) during the Viking Mission [*Kieffer et al.*, 1977]. The initial thermal inertia models were intentionally conservative, assuming a homogenous, flat-lying, unlayered surface. The model did allow CO_2 to condense and sublimate, and modeled atmospheric radiance as 2% of the noontime insolation [*Kieffer et al.*, 1977]. The IRTM data showed that thermal inertias range from 67 to about 460, and recognized regions of low thermal inertia and interpreted these areas to be covered with fine material and few exposed rocks. A strong anticorrelation between thermal inertia and albedo was also identified [*Kieffer et al.*, 1977]. *Palluconi and Kieffer* [1981] extended the work of *Kieffer et al.* [1977] to include a global map of thermal inertia at 2 pixels per degree using diurnal temperature measurements. They discussed the observed relationships between thermal inertia, albedo, and elevation, and confirmed the anticorrelation between albedo and thermal inertia. They also identified the basic global distribution of thermal inertia and albedo, and interpreted low thermal inertia/high albedo regions to be mantled in a layer of fine dust, and speculated on several scenarios, including a mixture of rock and fine sediment or the presence of crusts, to explain higher thermal inertia surfaces.

[9] *Christensen and Moore* [1992] presented Viking thermal inertia data using the same modeling technique as *Kieffer et al.* [1977], but used individual nighttime observations, rather than binned diurnal temperatures [*Palluconi and Kieffer*, 1981] allowing higher-resolution (30 km per pixel) mapping. This inclusion of additional data revealed the presence of small-scale (~30 km) thermal variations in all terrains, and fostered the identification of four global units based on thermal inertia and albedo. These units include: (1) active dust deposits; (2) active, coarse materials; (3) possible indurated surfaces; and (4) mixed coarse and dust materials, and these describe the majority of observed surfaces on Mars. In addition to these global thermal inertia maps, several regional studies have been performed using

Viking IRTM data in which the resolution and accuracy of the thermal inertia data set and the understanding of the local geology was improved [e.g., *Christensen and Kieffer*, 1979; *Zimbelman and Kieffer*, 1979; *Zimbelman and Leshin*, 1987; *Bridges*, 1994; *Hayashi et al.*, 1995].

[10] *Haberle and Jakosky* [1991] studied the effects of the atmosphere on thermal inertia calculations, and refined the atmospheric correction of *Kieffer et al.* [1977] by including a 16-layer atmosphere allowing a sensible energy exchange between the surface and the atmosphere. This improved atmospheric component resulted in reducing the thermal inertia values relative to those calculated by *Kieffer et al.* [1977] by as much as 25%, and further verified that low-inertia regions are likely mantled in dust deposited from the atmosphere. *Jakosky et al.* [2000] developed a model to calculate the thermal inertia using temperature data from the TES instrument. This model incorporates the atmospheric correction technique developed by *Haberle and Jakosky* [1991], and includes modifications to better account for the presence of CO_2 ground frost. Thermal inertia values range between 24 and 800 and results are typically within 50 units of those calculated with IRTM [*Jakosky et al.*, 2000]. *Mellon et al.* [2000] present a nighttime TES-derived bolometer-based thermal inertia map at 15 km per pixel resolution, with approximately 63% coverage between 50°S and 70°N latitude. They also divided the surface into three thermophysical units based on TES thermal inertia and albedo measurements, which include low thermal inertia and high albedo; high thermal inertia and low albedo; and moderate-to-high thermal inertia and intermediate albedo, and speculated on their origins. These divisions correspond well with those of *Christensen and Moore* [1992], and confirm the complex nature of Martian surface materials.

[11] *Putzig et al.* [2005] refined the work of *Mellon et al.* [2000] by including data from the entire MGS primary mapping mission, improving the spatial resolution to 3 km per pixel, and extending the global coverage to between 80°S and 80°N latitude. *Putzig et al.* [2005] also further subdivided the planet into seven thermophysical units, including the three units from *Mellon et al.* [2000]. A low-to-intermediate albedo unit is found exclusively in the south polar region, and is interpreted as a low-density material caused by the desiccation of near-surface ice. Very low albedo material is primarily observed in Syrtis Major, Acidalia, and part of Vastitas Borealis, and may indicate a lack of unconsolidated surface material in these regions. Very high thermal inertia surfaces are consistent with very coarse-grained material, highly indurated surfaces, or exposed bedrock. Finally, very high albedo regions likely represent areas composed of very fine surface dust [*Putzig et al.*, 2005].

2. Methodology

[12] Thermal inertia values from the THEMIS data set are derived using a single temperature measurement similar to previous orbital data sets, including Viking [*Kieffer et al.*, 1977; *Christensen and Moore*, 1992] and TES [*Jakosky et al.*, 2000; *Mellon et al.*, 2000]. Nighttime temperatures only are used in this study because the effects of albedo and sun-heated slopes have dissipated throughout the night, and the thermal contrast due to differences in particle sizes are at a maximum [e.g., *Kieffer et al.*, 1977; *Palluconi and Kieffer*, 1981; *Christensen*, 1982]. The brightness temperature of the surface is determined by fitting a Planck curve to band 9 (centered at 12.57 μm) calibrated radiance that has been corrected for instrumental effects. Band 9 brightness temperatures are used to approximate the surface kinetic temperature and define the target temperature because this wavelength range has the highest signal to noise ratio and is relatively transparent to atmospheric dust. Changes in the instrument response function during launch and orbit insertion were minimal [*Christensen et al.*, 2003a, 2004], and the nighttime temperatures are calibrated to within a precision of 1.2 K and an absolute accuracy of $\sim$2.8 K at night (at 180 K), as determined in this work. These temperature accuracies are similar to the $\sim$1–2 K accuracy measured with the Thermal Emission Spectrometer (TES) infrared bolometer on the Mars Global Surveyor (MGS) [*Christensen et al.*, 2001].

[13] The thermal model used is derived from the Viking IRTM thermal model [*Kieffer et al.*, 1977, Appendix 1], with the primary modification being the replacement of a constant atmospheric thermal radiation with a one-layer atmosphere that is spectrally gray at solar wavelengths, and the direct and diffuse illuminations are computed using a two-stream delta-Eddington model; the dust single-scattering albedo is set at 0.9 and the Henyey-Greenstein asymmetry factor is set at 0.5. The atmosphere is radiatively coupled to the surface using an appropriate thermal capacity, and the thermal radiation is assumed to be gray and isotropic with a fixed ratio of 2.0 for the visible-to-infrared opacity. Because the atmospheric opacity has a minor effect (less than 5%) on thermal inertia at night, the atmospheric correction adequately takes into account the effect of the atmosphere. An explicit forward finite-difference scheme calculates surface and subsurface temperatures by solving the heat conduction equation while satisfying a surface boundary condition that includes upward emission and downwelling thermal radiation, direct and diffuse insolation, and the latent heat of CO_2 if its saturation temperature is attained. The local CO_2 frost point is determined at each input using the local partial pressure computed for a specific elevation, season, and latitude. This model assumes lateral surface homogeneity and a Lambertian surface reflection. Subsurface layers increase in thickness exponentially with depth and are scaled to the diurnal skin depth, but in this work all layers are uniform in both composition and conductivity. The surface emissivity is assumed to be unity and the lower boundary is assumed to be insulating. The effects of three-dimensional blocks on the surface, condensate clouds, and the latent heat of water ice are not considered. This model can incorporate the effects of a radiatively coupled sloping surface at any azimuth, but for the nominal thermal inertia calculations, slopes are not considered.

[14] The THEMIS band 9 temperatures are converted to a thermal inertia by interpolation within a look-up table. An individual table was generated for each framelet (256 lines) by selecting values appropriate for the THEMIS framelet for six input parameters: latitude, season, local solar time, atmospheric dust opacity, elevation (atmospheric pressure), and albedo. Thermal inertia was varied from 24 to 3000 in each case. These input parameters were then used to

Table 1. THEMIS Nighttime Temperature Calibration

	Band 9 1-σ Noise Equivalent Spectral Radiance	NEΔT (at 180 K)
Signal-to-noise	2.72×10^{-6} W cm^{-2} str^{-1} μm^{-1}	1.15 K
Column-row correlated	1.06×10^{-6} W cm^{-2} str^{-1} μm^{-1}	0.5 K
Time-dependent change in focal plane temperature		4.3 K
IRF slope		4 K
Offset		−2 to +6 K
RSS total		**2.8 K**

calculate the model-derived surface kinetic temperature for the specified conditions and thermal inertia range using the thermal model described above, resulting in a table of model-derived surface temperatures as a function of thermal inertia. This table and the measured band 9 surface temperatures are then used to interpolate the THEMIS thermal inertia. Interpolation is performed on a pixel-by-pixel basis using season, latitude, and local solar time from spacecraft ephemeris. The remaining model input parameters are obtained from external data sets. The albedo is determined from the TES albedo binned at 8 pixels per degree [*Christensen et al.*, 1992]. Elevation is ascertained from the MOLA elevation [*Zuber et al.*, 1992; *Smith et al.*, 1999; *D. E. Smith et al.*, 2001] binned at 128 pixels per degree. Finally, the opacity is determined from the TES atmospheric dust opacity binned at 0.5 pixel per degree every 30° L_s. Data gaps in albedo, elevation, and dust opacity maps were filled using a linear interpolation between neighboring bins weighted by distance. TES atmospheric dust opacity was used for the first Martian year of MGS mapping when there were no global dust storms [*Smith et al.*, 2000; *M. D. Smith et al.*, 2001]. We assume that the amount of dust in the atmosphere is repeatable from year to year; this has been shown to be a reasonable approximation during seasons devoid of major dust storms [*Clancy et al.*, 2000; *M. D. Smith et al.*, 2001]. To convert the TES IR atmospheric dust opacity to the equivalent opacity at visible wavelengths (the input requirement of the thermal model), the IR opacity was multiplied by a visible/9-μm extinction opacity ratio of 2.0 [*Clancy et al.*, 1995].

[15] The look-up table includes a thermal inertia range of 24 to 3000, and values exceeding 1800 have been observed thus far in the mission. This thermal inertia range is significantly larger than that used in the TES standard model (maximum of 800), and allows the detection of exposures of consolidated materials or bedrock on the surface. The higher resolution of THEMIS, the fact that many regions on Mars saturated at the maximum value of thermal inertia in the TES model, and initial results from THEMIS nighttime temperatures suggesting the presence of bedrock [e.g., *Christensen et al.*, 2003a] required this extension of the thermal inertia range.

[16] Thermal inertia can be used to interpret an effective particle size of the surface [*Kieffer et al.*, 1973], and this particle diameter is determined using laboratory-derived relationships between conductivity and the particle size of homogenous spheres [*Presley and Christensen*, 1997b]. The effective particle diameter (d) is given by substituting Equation 17 from *Presley and Christensen* [1997b] that describes the relationship between conductivity and particle size

$$k = \left(CP^{0.6}\right)d^{(-0.11 \log P/K)} \quad (1)$$

into the thermal inertia equation, $I = (k\rho c)^{1/2}$, where C and K are the constants 0.0015 and 8.1×10^4 torr (to convert to mbar, multiply 1 torr by 1.333 mbar), respectively [*Presley and Christensen*, 1997b], P is atmospheric pressure in torr, and d is the particle diameter in μm. An atmospheric pressure of 3.9 torr (Mars average surface pressure of 5.2 mbar (520 Pa) at an $L_s = 0°$ [*Smith and Zuber*, 1998]) is used, and ρc is assumed to be 1×10^6 J m^{-3} K [*Neugebauer et al.*, 1971]. Equation (1) is valid for thermal inertia values less than ~350, and errors in deriving particle sizes with this method are expected to be less than 10–15% [*Presley and Christensen*, 1997b].

3. Thermal Inertia Uncertainties

[17] Sources of uncertainties in thermal model determinations include: (1) uncertainties in THEMIS nighttime temperatures; (2) model sensitivities due to uncertainties in surface parameters, such as albedo, obtained from external data sets; (3) look-up table interpolation residuals; and (4) atmospheric, surface, and subsurface physics not accounted for by the thermal model. Uncertainties are inherent in any model used, and important insight can be gained from these uncertainties as they provide the boundaries within which the model results can be interpreted. Uncertainties in THEMIS temperature measurements and derived thermal inertia values are discussed in detail in sections 3.1; relative differences between thermal inertia values within a single image have precision of 10–15% and the absolute value of thermal inertia is ~20%. A summary of the discussed uncertainties is listed in Tables 1 and 2.

Table 2. Thermal Inertia Image Uncertainties[a]

Precision	Assigned Uncertainty	Percent Contribution
Nighttime temperature	1.2 K	6%
Albedo	0.03	6%
Elevation	100 m	0.5–1%
Slopes	1°	3%
Interpolation	n/a	1–2%
Visible/9-μm extinction opacity ratio	1.5–3 K	10%
Unit emissivity	1.2 K	6%
Total		**11.5%**
Accuracy	**Assigned Uncertainty**	**Percent Contribution**
Nighttime temperature	2.9 K	16%
Albedo	0.03	6%
Elevation	100 m	0.5–1%
Atmospheric opacity	0.1	3%
Slopes	1°	3%
Interpolation	n/a	1–2%
Visible/9-μm extinction opacity ratio	1.5–3 K	10%
Unit emissivity	1.2 K	6%
Total		**21%**

[a]Because model parameters are uncorrelated, these values are combined using a Root Sum Square method. This result is then added to the average nighttime temperature calibration to acquire the total image uncertainty.

3.1. Measurement Uncertainties

3.1.1. THEMIS Nighttime Temperatures

[18] To quantify temperature uncertainties and establish the precision and accuracy of the THEMIS instrument calibration at night, the procedure used by *Bandfield et al.* [2004] for THEMIS daytime measurements was repeated for THEMIS nighttime temperatures. The THEMIS temperatures are determined from the difference between the radiance of the scene and the internal reference calibration flag measured in scaled, eight-bit "data numbers" (DN). There are several random and systematic factors that complicate the calibration of THEMIS data, and each one will be discussed individually in terms of its relevance to nighttime temperatures, and specifically the 12.57-μm-wavelength region (band 9).

3.1.1.1. Signal-to-Noise

[19] The 1 σ noise equivalent spectral radiance (NEΔR) for band 9 is 2.72×10^{-6} W cm^{-2} str^{-1} μm^{-1}, corresponding to a noise equivalent delta temperature (NEΔT) of 1.15 K at 180 K (P. R. Christensen, THEMIS calibration report, 2005, available at http://themis-data.asu.edu/pds/calib/calbi.pdf) (hereinafter referred to as Christensen, Themis calibration report, 2005). This error can be reduced by averaging pixels in an area when analyzing image data, increasing the signal-to-noise ratio.

3.1.1.2. Column-Row Correlated Noise

[20] Column-row correlated noise is caused by small changes in both the detector response relative to the prelaunch response function and minor fluctuations in detector readout bias voltage, and is identified as variations of ±1 DN along a row. This error corresponds to a NEΔR of $\pm 5.31 \times 10^{-6}$ W cm^{-2} str^{-1} μm^{-1} in band 9 and an NEΔT of ±2.2 K at 180 K, and is detected and reduced during standard image calibration to <0.2 DN [*Bandfield et al.*, 2004] (NEΔR of $\pm 1.06 \times 10^{-6}$ W cm^{-2} str^{-1} μm^{-1} in band 9 and an NEΔT of ± 0.5 K at 180 K), and can be further reduced by averaging pixels when analyzing image data.

3.1.1.3. Time-Dependent Change in Focal Plane Temperature

[21] The THEMIS focal plane substrate is temperature controlled to ±0.001°C (Christensen, Themis calibration report, 2005). However, the active surfaces of the microbolometer detectors change temperature in response to radiance from the surface. Temperature changes of ~0.001°C result in signal changes of 2 to 3 DN ("drift"). In addition, there are higher-frequency (1–5 s) variations in the output signal due to the actions of the focal plane temperature controller ("wobble"). These effects are reduced by assuming that the atmospheric temperature is constant throughout an image and that band 10 (centered at 14.88 μm, the fundamental CO_2 absorption) should therefore be constant. Changes in band 10 are assumed to be due to "drift" and "wobble" and these effects are removed from all other bands. The magnitude of this effect is typically ±5 DN at night [*Bandfield et al.*, 2004]. When the post-image calibration observation of the internal shutter/calibration flag is acquired within 120 s after the completion of the image, the total error after correction is estimated to be <2 DN for the first line of the image and zero for the last line of the image [*Bandfield et al.*, 2004], corresponding to an absolute error of 4.3 K at 180 K.

3.1.1.4. Instrument Response Function Slope Errors

[22] The THEMIS instrument response function (IRF) was defined prelaunch using measurements of blackbody targets at a range of temperatures in a vacuum chamber, and is constant over expected operational instrument temperatures [*Christensen et al.*, 2004; Christensen, Themis calibration report, 2005]. The accuracy of the IRF slope is within ~2% and was determined using comparative TES data, space observations, and CO_2 polar cap images [*Bandfield et al.*, 2004]. Using a surface temperature of 180 K and an instrument temperature of 270 K, errors in the IRF result in a maximum IRF slope error of 4 K.

3.1.1.5. Offset Errors and Shutter Closing Image

[23] Typical offset errors range from −1 to +3 DN [*Bandfield et al.*, 2004], which result in offset errors between −2 and +6 K at 180 K. In addition, a calibration image is acquired of the shutter/calibration flag after image acquisition to assess the temperature of the instrument; this value is used to set the instrument offset during calibration. Ideally, the calibration flag image is taken immediately following the planet image, but owing to software and data buffer constraints, it is typically delayed by ~60 s for nighttime data, resulting in a 1–2 DN error and a temperature error of 2.3 K at 180 K.

3.1.1.6. Absolute Calibration of Nighttime Images

[24] To assess the quality of THEMIS nighttime calibration considering all the above uncertainties, we calculated the surface temperature at 60 locations within nighttime THEMIS images over the southern CO_2 polar cap, and assessed if the measured temperatures are consistent with the expected saturation temperature of the latent heat of CO_2 (148 K). The difference between the expected temperature and the measured temperature ranged from 0.2 K to 18 K, and the X^2 of this difference was 7.5 K at 148 K. This result is consistent with a 1.8 K difference at 180 K. Considering the calibration factors discussed above, a reasonable estimate of the absolute accuracy of the THEMIS temperature calibration at night is between 1.8 K and 2.8 K. To assess the precision of the THEMIS instrument, we also determined the 1-σ NEΔR within each location and converted that value to an NEΔT at 180 K. This precision is 1.2 K, and corresponds well with the signal-to-noise value of 1.15 K reported by Christensen (Themis calibration report, 2005).

3.1.2. Model Sensitivity and Error Propagation

[25] A study was performed to determine the sensitivity of the thermal model to variations in albedo, elevation, dust opacity, and slopes and how these sensitivities propagate into uncertainties in the resulting thermal inertia values. In this assessment, one input parameter of the model was systematically varied for a range of latitudes and seasons, while all other parameters were held constant (sensitivity study input parameters are listed in Table 3). Only results where latitude was varied will be discussed, but similar uncertainties were calculated varying season as well. Because nighttime data alone were used in this work to calculate thermal inertia values, only errors for nighttime conditions (5 H) are reported, and are similar for all local times observed by the THEMIS instrument (3 to 6 H).

Table 3. Sensitivity Study Parameters

	Minimum	Maximum	Increment Value
Latitude	−90°	+90°	10°
Season	0°	360°	30°
Albedo	0.0	0.5	0.05
Elevation, km	−8.0	+8.0	1.0
Atmospheric dust opacity	0.0	1.0	0.05
Slope	0°	30°	variable
Slope azimuth	0°	360°	90°

3.1.2.1. Albedo

[26] Albedo primarily affects the average surface temperature and the phase of the diurnal temperature curve [*Kieffer et al.*, 1977], and is generally found to be inversely correlated to thermal inertia on Mars at all spatial scales [e.g., *Kieffer et al.*, 1977; *Palluconi and Kieffer*, 1981; *Zimbelman and Leshin*, 1987]. Uncertainties in the surface albedo are caused by differences between the true surface albedo as a function of wavelength and incidence angle and the model input value. This discrepancy can be due in part to uncertainties in the TES albedo data set, or from variations in albedo below TES resolutions affecting THEMIS surface temperatures. Error can also result from the assumption of a Lambertian surface in determining the TES albedo from a fixed viewing geometry and the fact that the Martian surface likely has a more complex photometric behavior.

[27] Higher-resolution THEMIS or MOC visible images may be helpful in identifying the presence of sub-TES-resolution variations in albedo, but quantifying these variations is difficult. Model sensitivities associated with thermal inertia as a function of albedo are illustrated in Figure 1a. An uncertainty in albedo of 0.03 for an albedo of 0.2, results in an error in thermal inertia of 6% to 10% for thermal inertias of both 80 and 600. Albedo has a larger effect on surface temperature at latitudes closer to the equator because in those regions the sun is above the horizon longer and later into the evening resulting in less nighttime hours to dissipate the effect of albedo on surface temperature, and thus thermal inertia.

3.1.2.2. Elevation

[28] Elevation is used to derive the atmospheric pressure, which is important for determining the average surface grain diameter from thermal inertia because of the pressure dependency of gas conductivity in small pores in the soil. Elevation also affects the relative amount of atmosphere above the surface, and thus the absorption of infrared energy and attenuation of energy through the atmosphere [e.g., *Kieffer et al.*, 1973; *Zimbelman and Kieffer*, 1979; *Haberle and Jakosky*, 1991; *Bridges*, 1994]. A correction for atmospheric pressure is included in the thermal model, and the uncertainties due to elevation are therefore small. The primary uncertainty is due to the spatial scale of the gridded MOLA topography relative to an individual THEMIS pixel. Model sensitivities of thermal inertia associated with elevation are illustrated in Figure 1b. Assuming an uncertainty of 100 m (MOLA binned at 128 ppd) at an elevation of 0 km, errors associated with elevation range from 1% for a thermal inertia of 80 to 0.5% for a thermal

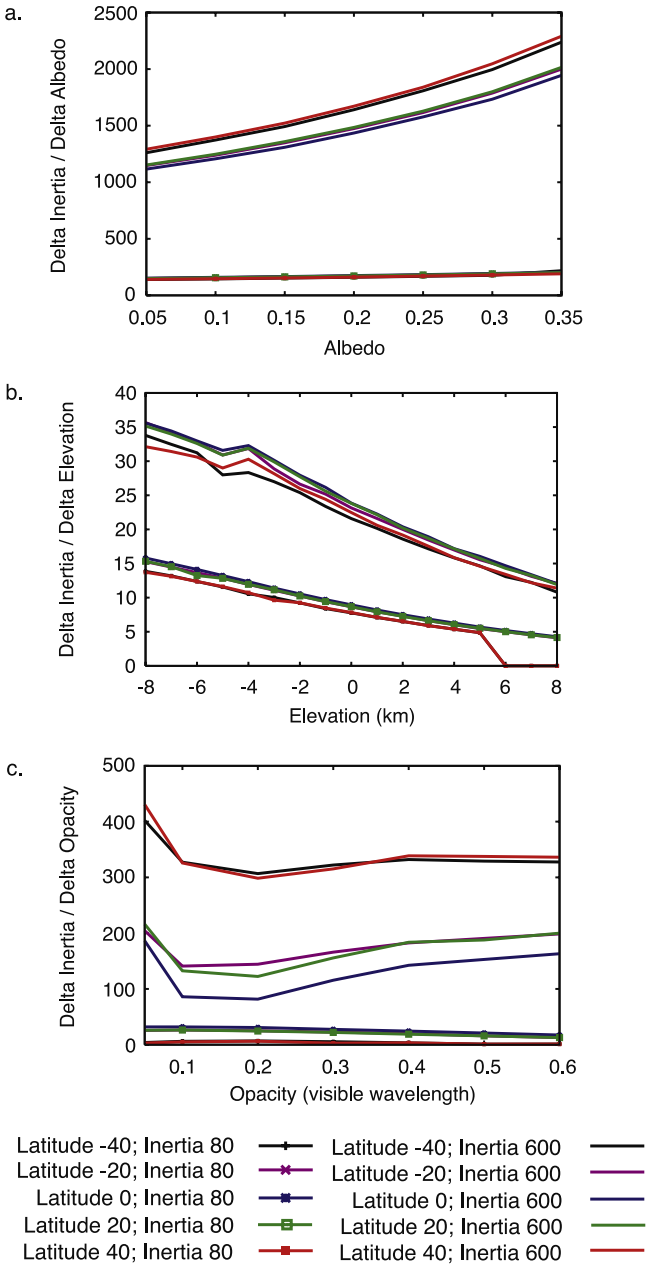

Figure 1. Thermal model input parameter sensitivities. Plots of the sensitivity of thermal inertia to variations in (a) albedo; (b) elevation; and (c) atmospheric dust opacity for a range of latitudes, a local time of 5 H, and an Ls = 0°. The curves with symbols are calculations for a thermal inertia of 80, the solid lines represent thermal inertia values of 600, and different colors represent different latitudes. Uncertainties for thermal inertia values between 80 and 600 can be approximated by linearly interpolating between these curves. To determine the uncertainty due to any input parameter, move across the *x* axis to the input parameter value that best characterizes the surface of interest. Then move vertically until the line best representing the thermal inertia and latitude is intercepted. Then move horizontally to intercept the *y* axis; this value is the partial derivative with respect to thermal inertia. Multiply this derivative value by the amount of uncertainty in the input parameter. The resulting value is the corresponding error in thermal inertia.

inertia of 600, depending on the latitude. The influence of elevation on temperature is larger for low elevations.

3.1.2.3. Atmospheric Dust Opacity

[29] The primary effect of additional dust in the atmosphere is to block solar energy from being incident onto the surface, increase the downwelling atmospheric thermal emission, and insulate the surface by preventing energy from escaping through the atmosphere [*Pollack et al.*, 1979]. Dust in the atmosphere damps the amplitude of the diurnal temperature variation, mimicking a higher thermal inertia surface [*Haberle and Jakosky*, 1991]. Overall, however, atmospheric dust opacity has a relatively small effect on thermal inertia calculations for several reasons. First, at night the surface and atmospheric temperatures are similar, and therefore small variations in the atmospheric temperature induce only small changes in the surface temperature. Increasing the amount of dust in the atmosphere increases the nighttime surface temperature by less than 1 K per 0.1 increase in visible opacity at a thermal inertia of 200 [*Fergason et al.*, 2006]. In addition, at relatively low opacities the atmosphere only absorbs a small percentage of solar energy, and small changes in opacity produce minor changes in the amount of energy incident upon the surface (periods of relatively high opacity ($\tau > 0.4$) are not used to determine thermal inertia). Finally, dust opacity does not vary dramatically spatially, and variations are largely seasonally repeatable from year to year [*Clancy et al.*, 2000; *M. D. Smith et al.*, 2001]. Uncertainties in the thermal inertia due to opacity errors occur when the actual opacity at the time the THEMIS image was acquired differs from the opacity at the season of image acquisition for a typical Mars year. An uncertainty in dust opacity of 0.1 at an opacity of 0.2, results in an error in thermal inertia of ~1% for thermal inertias of 80, and 2% to 7% for thermal inertias of 600, depending on the latitude (Figure 1c). The uncertainties are symmetrical about the equator, and increase towards the north and south poles.

3.1.2.4. Local Slopes

[30] Local slopes are not considered in the nominal method for determining thermal inertia with THEMIS data because high-resolution slope maps are not available to incorporate these data in an automated fashion. However on a larger scale, slopes can be incorporated on a framelet (256 lines) basis in the derivation of thermal inertia when necessary. Slopes are important because a sloped surface receives a different amount of incident thermal energy relative a horizontal surface. In addition sloped surfaces radiate onto a hemisphere that includes surface materials, rather than to a hemisphere of only sky for a flat-lying surface. The effect of slopes on thermal inertia was determined for slopes of 5°, 10°, 20°, and 30° at azimuths of 0°, 90°, 180°, and 270° (0° is North) (Figure 2). Assuming an uncertainty in slope of 1°, errors in thermal inertia range from 3% to 20%, depending on the slope and azimuth (Figure 2). Slopes facing west and east typically have a larger uncertainty than slopes facing north or south, primarily because more (or less) thermal energy is absorbed by surfaces at this orientation during the afternoon. However north or south-facing slopes can also be problematic because the sun can be incident on the surface for a dissimilar amount of time before and after 12 H, depending on the season and the latitude.

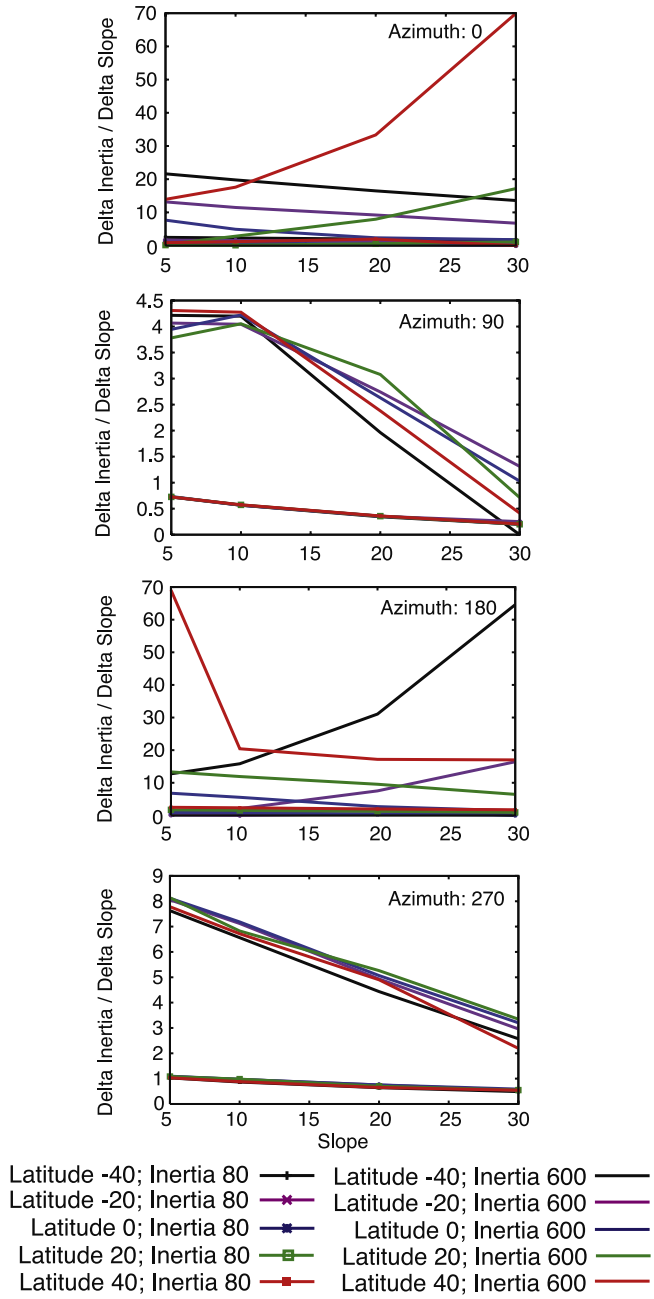

Figure 2. Thermal model slope input parameter sensitivities. Plots of the sensitivity of thermal inertia to variations in local slopes for a range of latitudes, a local time of 5 H, and an Ls = 0°.

[31] To further investigate the effect of slopes on temperature, and thus thermal inertia, we analyzed 12 surface nighttime temperature pairs along the walls of Valles Marineris, craters, and mesas with slopes ranging from 10° to 30° and at a range of azimuth orientations. THEMIS nighttime temperatures of opposite facing slopes were compared for each feature to determine the temperature difference, in order to quantify the residual effect of slopes at night. With only one exception out of these 12 examples, the temperatures of slopes with different orientations were the same to within ~3 K, which is about twice the

Table 4. Comparison of THEMIS Thermal Inertia Measurement of the Same Location

Location	Latitude	Longitude	Image ID	Thermal Inertia	Season (L_s)	Local Time	Albedo	Dust Opacity (Visible)	Elevation (km)
Meridiani Region 1	3.6°S	352.5°E	I11216001	210	52	4.9	0.15	0.2	−1.92
			I12439002	130	96	5.3	0.14	0.14	−1.63
			I06935007	245	218	5.4	0.14	0.56	−1.08
Meridiani Region 2	3.2°S	352.5°E	I11216002	275	52	4.9	0.14	0.2	−1.73
			I12439002	185	96	5.3	0.15	0.28	−1.68
			I06935007	310	218	5.4	0.15	0.56	−1.35
Meridiani Region 3	0.5°N	352.0°E	I01018006	450	339	3.1	0.23	0.42	−1.92
			I11216002	320	52	4.9	0.23	0.2	−1.55
			I12439002	310	96	5.3	0.23	0.24	−1.69
			I06935007	420	218	5.4	0.23	0.56	−1.92
Meridiani Region 4	5.6°N	351.6°E	I01018006	270	339	3.1	0.22	0.40	−1.95
			I01717002	180	8	3.4	0.22	0.22	−1.95
Gusev Region 1	11.3°S	174.9°E	I01511006	255	360	3.4	0.26	0.38	−1.78
			I08589007	140	303	4.3	0.26	0.34	0.59
Gusev Region 2	9.5°S	174.7°E	I01511006	130	360	3.4	0.26	0.40	0.59
			I08589007	55	303	4.3	0.26	0.38	−1.48
Arabia	2.9°N	26.4°E	I01229007	75	348	3.2	0.26	0.56	0.21
			I07895014	120	267	4.8	0.27	0.94	0.12
Isidis Region 1	12.8°N	84.5°E	I06732011	255	207	5.4	0.23	0.30	−3.9
			I09815012	210	358	4.2	0.23	0.28	−3.9
Isidis Region 2	17.2°N	83.9°E	I06732011	270	207	5.4	0.24	0.22	−3.79
			I09815012	210	358	4.2	0.24	0.28	−3.79

NEΔT of the instrument. In some cases, differing geology such as more rocky material on one wall complicated the measurement and made confirmation difficult, but these results suggest that any additional heat absorbed by the sloped surface during the day has sufficiently dissipated at night to have little effect on the derived thermal inertia. Generally, slopes below 10° at all azimuths had a small effect on the surface temperature, and therefore the thermal inertia at night. Higher slope angles may not be problematic, but this conclusion is dependent on the slope azimuth and the season. Owing to the potential for slopes to be a factor, surfaces with slopes greater than ~10° should include slope measurements in the thermal inertia derivation and be interpreted with caution.

3.1.2.5. Additional Uncertainties

[32] Additional uncertainties include errors in interpolation within the look-up table, assuming a constant visible/9-μm extinction opacity ratio, and assuming a surface emissivity of unity. When creating the look-up table, the node values were intentionally selected to minimize the errors due to interpolation; these errors are less than 1–2%.

[33] A constant visible/9-μm extinction opacity ratio of 2.0 was used in this work, but this ratio may vary between ~2.0 and ~2.5 for visible atmospheric dust opacity conditions below 1.0 [*Clancy et al.*, 1995]. Increasing the visible/9-μm extinction opacity ratio increases the modeled temperature at all times of day with a greater effect at night. Varying visible/9-μm extinction opacity ratio from 2.0 to 2.5 changes the modeled surface kinetic temperature ~1.5 K at night for low opacity conditions (τ = 0.2) and ~3 K at night for high opacity conditions (τ = 0.6), producing an uncertainty of ~10% in thermal inertia.

[34] Finally, a constant unit emissivity is assumed for this work. Any constant emissivity used is an assumption because different surface materials have different emissivity values. A unit emissivity was chosen because it is the simplest case and is a reasonable assumption in most instances. This effect is not significant as changes in the emissivity from 1.0 to 0.96, which is typical for Mars at 12.57 μm (band 9) [e.g., *Bandfield*, 2002], only changes the surface kinetic temperature 1.2 K, which translates to a ~6% change in thermal inertia.

3.2. Repeatability of THEMIS Thermal Inertia Determinations

[35] Considering the uncertainties and conditions that may affect the reliability of thermal inertia calculations, it is instructive to compare multiple images of the same location to quantify the repeatability of THEMIS thermal inertia measurements and to determine how well the thermal inertia model is correcting for seasonal, local time, and atmospheric dust opacity differences in data acquisition. Many areas on the Martian surface, especially those of high scientific interest such as the candidate MER landing sites, have been observed multiple times at night with the THEMIS instrument over a range of conditions. Thermal inertia images from regions in Meridiani Planum, Gusev Crater, Arabia Terra, and Isidis Planitia were selected for comparison (Table 4). To increase the signal to noise ratio, several hundred pixels were added together in each comparison. Of the images selected, the thermal inertia differences for the same location ranged from 12 to 120, with an average difference of 65, corresponding to an overall agreement between images of ~35%.

[36] The difference between THEMIS thermal inertia values is likely due to a combination of model input parameter uncertainties and an incomplete understanding and incorporation of surface-atmospheric interactions. The image-to-image variation is higher than the estimated accuracy of the THEMIS thermal inertia calculation (Table 2), and thus it is also probable that some of these differences are due to real variations in nighttime surface temperature caused by day-to-day variations in haze or near-surface winds, or surface and subsurface heterogeneities not accounted for by the thermal model. It should be noted, however, that although image-to-image comparisons have

errors of ~35%, relative differences within a THEMIS image are 10% to 15%. Relative differences in a single image are calibrated to within ~1.2 K, and any uncertainties in data calibration affect the entire image in a consistent manner.

3.3. Summary of Uncertainties

[37] The accuracy of THEMIS-derived thermal inertia values is separated into two categories: (1) the absolute accuracy of THEMIS-derived thermal inertia values and (2) the relative precision of thermal inertia values within a single image. The calibration of the THEMIS instrument is the largest factor in determining the absolute accuracy of thermal inertia calculations. Knowledge of model input parameters such as albedo, elevation, and local slopes also play a role, but the combined contribution of all these errors is roughly equal to that of the instrument (Table 2). Factors such as assuming a visible/9-μm extinction opacity ratio of 2.0 and a surface emissivity of unity may also be contributing to the thermal inertia uncertainties, but their presence and contribution is difficult to quantify. Overall, absolute accuracy of THEMIS-derived thermal inertia is ~20% (Table 2). The precision of temperature measurements within an individual THEMIS image is ~1.2 K. The relative differences between thermal inertia values within a single image have a precision of 10–15% (Table 2). Individual thermal inertia images are important for determining variations in thermal inertia between small-scale surface features, and thermal inertia variations across these images represent true differences in the physical properties of the surface.

4. Comparison with Previous Orbital and Lander Data

4.1. Comparison with the Thermal Emission Spectrometer

[38] Differences between the TES- and THEMIS-derived thermal inertia values are expected, and are caused by several factors including differences in the capabilities of the instruments, the method of calculating surface temperature, and the thermal models employed. The TES instrument measures the surface temperature of Mars using both an infrared spectrometer (5.8 to 50 μm) and a broadband thermal radiometer (5.1 to ~100μm) [*Christensen et al.*, 1992, 2001]. For the TES spectrometer, the radiance at each wavelength is converted to brightness temperature assuming an emissivity of unity. The maximum brightness temperature (away from the CO_2 band) is assumed to be the surface kinetic, or target, temperature [*Christensen et al.*, 2001]. Planetary (top of the atmosphere) brightness temperatures are calculated using the TES bolometer by measuring the total emitted radiance from the Martian surface and determining the temperature of an ideal blackbody corresponding to this total radiance. At night, the planetary temperature is typically 3–4 K lower than the target temperature due to the presence of the 15-μm CO_2 absorption band that reduces the integrated radiance when the atmosphere is colder than the surface. Despite larger calibration uncertainties with the TES spectrometer than the bolometer, the target temperatures are likely the most accurate measurement of surface temperature because the effect of the atmosphere on the target temperature is well understood. *Jakosky et al.* [2000] and *Mellon et al.* [2000] derived thermal inertia values from both spectral and bolometric temperatures. Rather than using target temperatures measured by TES to calculate spectrometer-based thermal inertias, they use a Viking-IRTM-equivalent 20-μm-band temperature. This method was chosen to avoid interference from atmospheric dust or clouds and to allow easily comparable results with IRTM-derived thermal inertia values [*Mellon et al.*, 2000]. The bolometer-based thermal inertias were calculated using brightness temperatures, correcting for the 15-μm CO_2 absorption band [*Mellon et al.*, 2000].

[39] THEMIS uses a microbolometer detector with a smaller wavelength range than TES, and this instrument design requires a different method for deriving surface temperature than discussed above. A look-up table of Planck curve temperatures is calculated for the wavelength region of each band, and this look-up table is used to calculate the brightness temperature measured by THEMIS for each filter. Rather than defining the surface kinetic temperature as maximum brightness temperature of all wavelength bands as with TES, at night band 9 (centered at 12.57 μm) has the highest brightness temperature and provides the best approximation of the surface kinetic temperature [*Christensen et al.*, 2004]. However, the surface emissivity at this wavelength is likely to be less than unity, and this temperature does not directly correspond to either temperature used in the analysis of TES data.

4.1.1. Comparison of Thermal Inertia Modeling Techniques

[40] In addition to differences in the instruments and methods for deriving surface temperatures, different thermal models are also utilized when deriving the TES and THEMIS thermal inertia values. The primary difference between these models is in the treatment of the atmosphere. Both models account for radiation through a dusty CO_2 atmosphere and allow for heat exchange with the surface. However, the thermal model used in this work incorporates a one-layer atmosphere that is spectrally gray at solar wavelengths, and direct and diffuse illuminations are computed using a two-stream delta-Eddington model. The thermal model used in the derivation of TES thermal inertia values includes a 16-layer atmosphere [*Haberle and Jakosky*, 1991], and incorporates the vertical transfer of energy through the atmosphere due to convective overturning within the boundary layer [*Jakosky et al.*, 2000; *Mellon et al.*, 2000]. The different atmospheric corrections produce slight differences in the amount of thermal energy incident on the surfaces, and the models may respond differently to atmospheric dust.

[41] To understand these differences in the thermal models used for TES and THEMIS, we compared the two thermal models as directly as possible. The TES thermal inertia production look-up table was replicated using the thermal model used in this work by using the same input parameter nodes (season, local time, latitude, elevation, thermal inertia, albedo, and atmospheric dust opacity) in the thermal model and comparing the resulting temperature values with those in the TES thermal inertia production look-up table. The thermal model temperatures agree to within ~3 K for a range of typical surfaces, dust opacities, latitudes, and seasons (Figure 3), indicating that any differences between the thermal models does not significantly

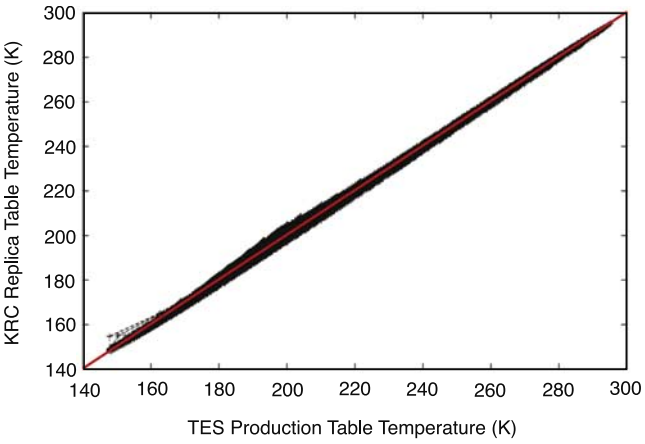

Figure 3. KRC replica table temperatures compared to TES production table temperatures. The thermal model utilized in this work (KRC) was used to replicate the TES thermal inertia production look-up table to allow a direct comparison between the thermal models. These data are compared for a representative thermal inertia of 248, albedo of 0.25, atmospheric dust opacity of 0.50, all seasons, and latitudes from 40°S to 40°N. The red line indicates a perfect agreement between the thermal models. Other thermal inertia and albedo values produce similar results.

contribute to differences between TES and THEMIS-derived thermal inertia values.

4.1.2. Comparison of Thermal Inertia Maps

[42] The comparison of TES and THEMIS-derived thermal inertia values ±40° from the equator, due to sparse THEMIS coverage between ~40° and 60° latitude, and binned at 2 pixels per degree, is shown in Figure 4. THEMIS thermal inertia values are compared to TES bolometric thermal inertia values, because these TES values incorporate TES surface temperature measurements and are therefore believed to be the most accurate representation of the physical nature of the surface as measured by TES. To construct the global THEMIS thermal inertia map, THEMIS thermal inertia data were averaged in a single image every 256 lines (framelet, effectively 32 × 26 km) and this information was stored in a database along with longitude, latitude, and information about the image calibration and processing quality. Nighttime images selected for this map have a high quality of calibration, have emission angles less than 30°, are from a period where there are no global dust storms, and have no surface CO_2 frost present. The average thermal inertia for each framelet was binned at 2 pixels per degree and gaps in the data were filled using a linear interpolation between neighboring bins weighted by distance.

[43] To create the TES thermal inertia map, the TES thermal inertia data were constrained to have incidence angles greater than 95°, emission angles less than 30°, a high quality of thermal inertia derivation, and only seasons with a low dust opacity and no equatorial water-ice clouds were included. This TES thermal inertia map is similar to the published TES global maps of *Mellon et al.* [2000] and *Putzig et al.* [2005], but the effect of H_2O-ice clouds in the low inertia equatorial regions has been reduced and the elevated thermal inertia values in the northern polar region have been excluded. The THEMIS and TES-derived global thermal inertia maps agree to within 25–30%, and the familiar thermophysical features, such as the low thermal inertia areas of Tharsis Montes, Elysium Planitia, and Arabia Terra and the higher thermal inertia regions of the southern rim Isidis Planitia and Valles Marineres, are consistent. A scatter plot and histogram (Figures 5a and 5b, respectively) of THEMIS and TES thermal inertia values both illustrate that THEMIS-derived thermal inertia values are typically higher than those derived with TES data for an individual location. In addition, there is more variation in thermal inertia values in the low thermal inertia regions in the THEMIS data set. To ensure global coverage, the THEMIS thermal inertia map incorporates data spanning an entire Mars year, whereas the TES map only includes data from L_s 30° to 60°, when the presence of global atmospheric dust and H_2O-ice clouds in the equatorial regions are minimized. Seasonal variations in surface temperature or atmospheric conditions, including the presence of H_2O-ice clouds, may be causing the variation in the low thermal inertia regions observed in THEMIS data. Time of day effects not accounted for in the thermal model may also be present, since THEMIS and TES data incorporated were acquired at local times ranging from ~3.5 H to ~5.5 H and ~2 H, respectively.

[44] The highest thermal inertia areas found in Valles Marineris, the southern rim of Isidis Planitia, the outflow channels of Xanthe Terra, and Acidalia Planitia are similar in two data sets, but THEMIS shows less areal abundance of high thermal inertia material (Figure 4). This difference is more pronounced because of the stretch applied to the data, and actual differences are ~15%. This is likely due in part to a lower than unity emissivity in these regions. Most high thermal inertia areas on Mars have a lower albedo, and these lower albedo surfaces can have an emissivity as low as ~0.97 in THEMIS band 9 (12.57 μm). The THEMIS thermal model assumes an emissivity of unity, and this discrepancy will result in a lower estimation of the thermal inertia in these regions by ~6%. The TES thermal model also assumes an emissivity of unity, but this issue is not a problem with the bolometer data. Different atmospheric conditions and local times may also be contributing factors.

[45] In addition, image-to-image variations in thermal inertia due to seasonal atmospheric variations not accounted for in the thermal model are also present in the THEMIS map resulting in a "stripy" appearance. Because the seasonal range used to create the TES map is more narrowly constrained and TES collects data continuously whereas THEMIS images are targeted, there is more consistent nighttime coverage of the planet with the TES data set resulting in a cleaner, less "stripy" thermal inertia map. Both the thermal models used and the thermal inertia values produced agree to within 25–30%, and this discrepancy is caused by a variety of factors, including differences in the: (1) instrument, and thus the temperature measurements; (2) thermal model; (3) seasonal atmospheric conditions; and (4) local times the data were acquired. The classification of surface particle sizes used in geologic interpretations is often divided based on the Wentworth Grade Scale [*Wentworth*, 1922], and this dissimilarity in thermal inertia values is sufficiently small to allow one to differentiate

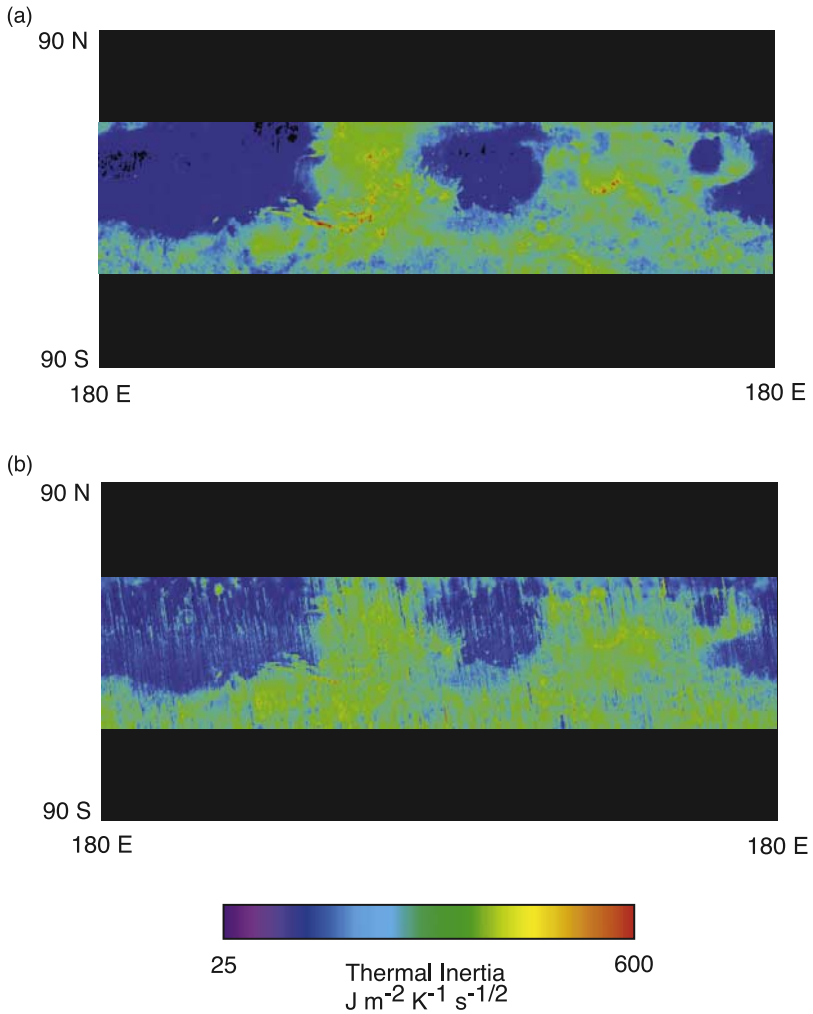

Figure 4. Global thermal inertia maps. (a) TES-derived thermal inertia (30 km per pixel; 2 pixel per degree resolution). (b) THEMIS-derived bolometric thermal inertia (30 km per pixel; 2 pixel per degree resolution).

these common particle size classes (such as silt versus sand). Therefore this difference does not effect the discrimination of major surface types (i.e., dust, sand, rock) or the interpretation of the physical nature of the Martian surface.

4.2. Comparison with Mini-TES Surface Measurements

[46] Surface temperatures obtained by the Mini-TES instrument at the MER-Spirit landing site region at Gusev Crater were used to derive thermal inertia values [*Fergason et al.*, 2006], and provides an opportunity to corroborate the THEMIS-derived thermal inertia data. Along the traverse from the Columbia Memorial Station landing site to Bonneville crater, the thermal inertia in both the Mini-TES and THEMIS data sets increased from 175 ± 20 to 380 ± 20 and 280 ± 40 to 330 ± 40, respectively (Figure 6). This increase is likely caused by additional centimeter-sized rock fragments and a higher rock abundance in the Bonneville crater ejecta [*Golombek et al.*, 2005; *Fergason et al.*, 2006]. From Bonneville crater to the Columbia Hills, the THEMIS and Mini-TES thermal inertia values show similar thermal inertia patterns; Mini-TES values being on the average 20% lower and showing greater variation [*Fergason et al.*, 2006]. Larger variations in the Mini-TES data are expected as the spatial resolution is typically 100-fold higher than THEMIS. The lower Mini-TES thermal inertias may also be due to a data bias, as the rover avoided obstacles, such as rocks or bed forms, during the traverse and the Mini-TES observations were acquired directly in front of the rover [*Fergason et al.*, 2006].

5. Applications

[47] THEMIS-derived thermal inertia permits the characterization of the physical nature of surface materials observed in high-resolution images. Features observed in MOC and THEMIS visible images can often be uniquely associated with a distinctive thermal inertia at THEMIS resolution, and thus the physical nature of the surface materials can be determined. Dusty surfaces, bed form material, interior layered deposits, and exposures of surface bedrock have been examined to: (1) identify the thermal inertia and effective particle size of landforms and features in THEMIS and MOC images to aide in the interpretation of

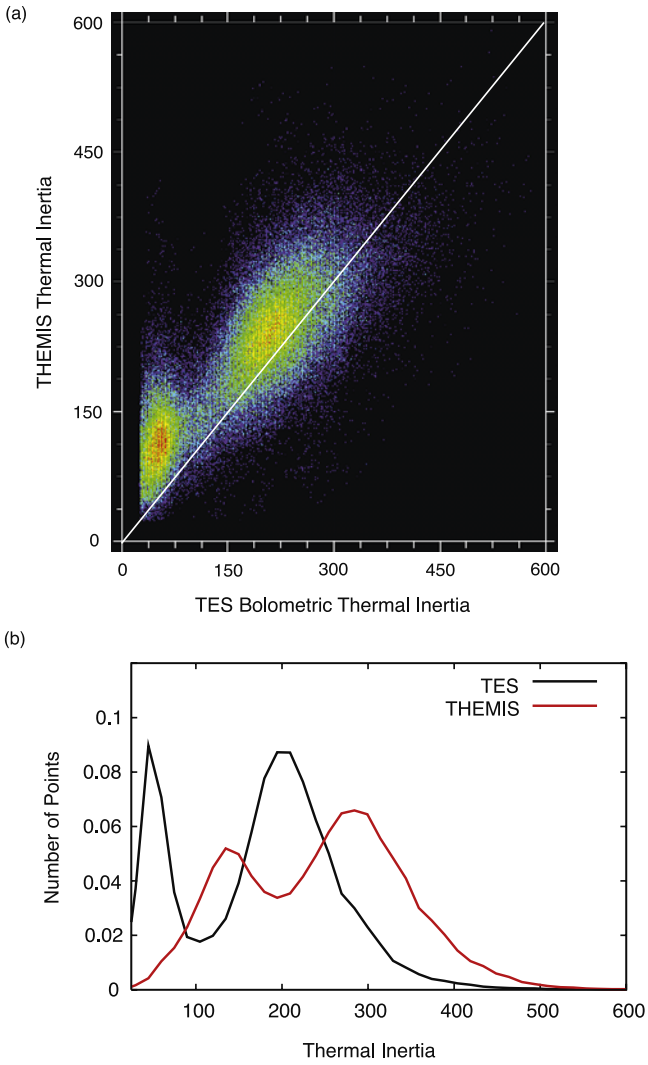

Figure 5. Global thermal inertia scatterplot and histogram. (a) Two-dimensional scatter plot of THEMIS and TES thermal inertia values. The while line indicates the x = y line of perfect agreement between the data sets. Red indicates a high frequency, whereas purple indicates a frequency of 1. (b) Histogram of THEMIS and TES derived thermal inertia values.

these regions; and (2) combine this information to better understand the geologic history and processes that have affected the Martian surface.

5.1. Dust Mantled Surfaces in Tharsis Montes

[48] Tharsis Montes is one of the classic low thermal inertia regions on Mars and is interpreted to have a surface layer of unconsolidated air-fall dust less than ~2 m thick [*Christensen*, 1986]. Tharsis was first identified as having a very low thermal inertia in Viking IRTM data [*Kieffer et al.*, 1977; *Zimbelman and Kieffer*, 1979; *Palluconi and Kieffer*, 1981] at a resolution of ~120 km per pixel. The improvement in resolution of the TES data set confirmed the pervasive nature of this low thermal inertia material at a resolution of 3–5 km per pixel [*Mellon et al.*, 2000]. As a type example of dust-covered surfaces on Mars, a region 600 km × 1120 km in Tharsis Montes centered at 260.5°E, 7°N (Figure 7) was studied using THEMIS thermal inertia values and THEMIS and MOC visible images. This region was analyzed to determine if this dust mantle is also homogeneous at 100 m per pixel resolution or if features, such as individual lava flows, observed in high-resolution visible images can be distinguished thermally.

[49] This region has both a uniform THEMIS (90–115) and TES (60–80) thermal inertia and a TES albedo of 0.29–0.30, indicating the presence of a surface layer of dust greater than a few centimeters thick. The dust cover index (DCI; 0.93–0.94) also indicates that a surface layer of fine, unconsolidated material is present [*Ruff and Christensen*, 2002]. In visible images individual lava flow fronts and wrinkle ridges are observed, and distinctive lava flow textures and the level of surface degradation suggest that individual flows are from different eruptive events. Topographically lower layers often have a more uniform texture, indicating that they are likely older and more degraded. This region displays erosional surfaces both at THEMIS and MOC resolution, such as the lack of crater ejecta, the erosion of lava flow fronts, and knobby lava flow textures, suggesting that a surface layer has been removed. In some cases, the surface morphology appears smoothed, particularly at MOC resolution, indicating the likelihood of a dust mantle on the surface.

[50] Despite the presence of visible lava flow fronts and differences in lava textures on these surfaces, there are no thermal inertia variations at THEMIS resolution associated with individual lava flows or the distinctive surface textures observed in visible images. The homogeneous nature of THEMIS thermal inertia values in this area indicates that the dust layer must have a minimum thickness sufficient to mask the thermal signature from underlying material (a few centimeters), but is still thin enough to be able to distinguish small craters (10–500 m in diameter) and surface textures at the resolution of MOC visible images. Assuming a depth: diameter ratio of 1:5 to 1:3 for simple craters [*Melosh*, 1989, p. 126], the smallest craters observed are 2–3 m deep; thus more than a few meters of dust would obscure these features. Also, in THEMIS visible images (18 m per pixel) it is difficult to discern the presence of a dust mantle, but in MOC images (~3 m per pixel) surface morphologies often appear smoothed or mantled, further indicating that the dust mantle is less than several meters thick. These observations indicate that although unconsolidated dust is present on the surface, it cannot be more than 1–2 m thick, and is likely thinner in many localities. Dust may currently be depositing in this region [e.g., *Zimbelman and Kieffer*, 1979; *Palluconi and Kieffer*, 1981; *Christensen*, 1986; *Christensen and Moore*, 1992], but likely some process, such as dust devils or wind erosion [*Christensen*, 1982], is allowing for the removal of that dust so that over time there is a net balance of dust accumulation and removal in this region, preventing tens to hundreds of meters of dust accumulation.

5.2. Bed form Material

[51] The Martian surface is currently dominated by aeolian activity [e.g., *Malin and Edgett*, 2001], and aeoilan bed forms are observed in visible images in a variety of terrains and geologic settings on Mars. Within a crater centered at 63°E, 26.5°N, surfaces that have eroded into mesas, knobs,

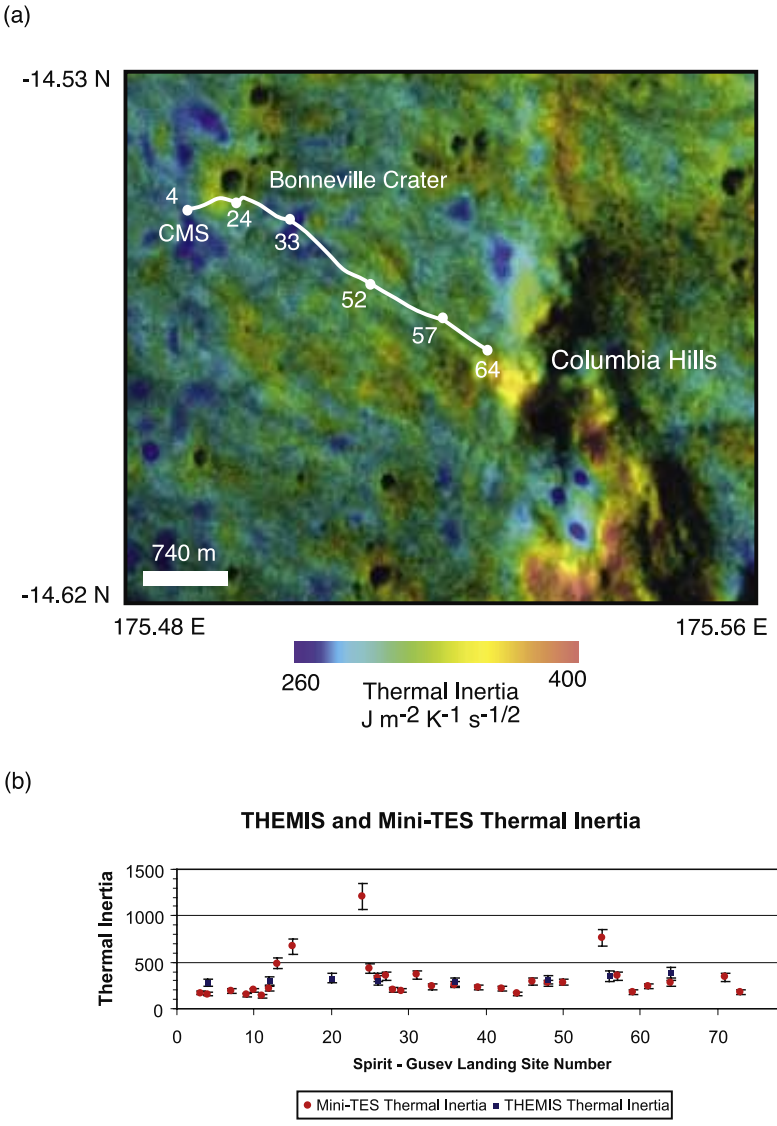

Figure 6. Comparison of THEMIS-derived orbital and Mini-TES-derived surface thermal inertia values. (a) THEMIS thermal inertia map (100 m per pixel resolution) overlaid onto a THEMIS visible image (18 m per pixel resolution) from Columbia Memorial Station (CMS) to Bonneville crater to the Columbia Hills at the Gusev crater landing site region. (b) Comparison of THEMIS-derived orbital and Mini- TES-derived surface thermal inertia values plotted. Modified from *Fergason et al.* [2006, Figures 8 and 13].

and ridges (Figure 8, A units) have a THEMIS thermal inertia of 420 to 465 in contrast to the lower thermal inertia of aeolian material (Figure 8, B units). Isolated areas of this higher inertia unit are too small to be resolved in the TES thermal inertia data set. The higher THEMIS thermal inertia and the presence of features resistant to erosion indicate that this surface is consolidated or lithified, and may be bedrock material intermixed with varying amounts of unconsolidated sand, resulting in a lower thermal inertia than is expected for exposed bedrock. There are at least four layers of material observed in MOC and THEMIS visible images, further indicating that these layers have been eroded or stripped to expose underlying units.

[52] The aeolian material (Figure 8, B units) has three morphologic expressions: (1) a low albedo material with bed forms (B_1); (2) a low albedo sheet that does not have bed forms at THEMIS visible resolution (18 m per pixel) (B_2); and (3) material present between consolidated surfaces (B_3). The bed forms and the sheet (Figure 8, B_1 and B_2 units) have a THEMIS thermal inertia of 230 to 270 (particle diameter of 290 to 575 μm corresponding to medium to coarse sand), and have a TES albedo of 0.11 to 0.12 and a DCI of 0.98. The particle size range implied by the thermal inertia is consistent with grains that can saltate under current atmospheric conditions [e.g., *Greeley et al.*, 1980], and the albedo and DCI indicate that little or no dust is present on the surface. The grain diameter, albedo, and DCI all suggest that these materials are active.

[53] The material present between mesas, knobs, and ridges (Unit B_3 in Figure 8) has a TES thermal inertia of

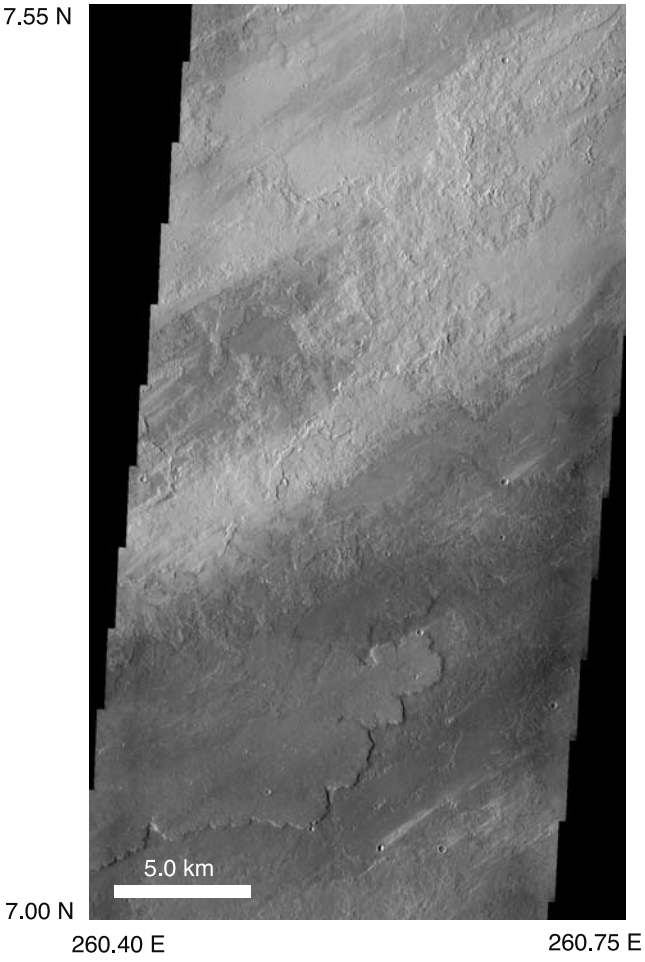

Figure 7. THEMIS visible image V10264011 of dust-mantled lava flow features in Tharsis Montes. In this region, the variation in TES albedo ranges from 0.29–0.30, and thus light and dark patterns are primarily a result of the stretch applied to the image, rather than true differences in albedo.

300 to 330 and a THEMIS thermal inertia of 230 to 340 (particle diameter of 290 to 1500 μm corresponding to medium sand to granules), and has an albedo comparable to the surrounding material. In addition, lighter toned bed forms that resemble transverse aeolian ripples (TARs) [*Malin and Edgett*, 2001; *Wilson and Zimbelman*, 2004] are often observed in topographic valley regions. The higher thermal inertia range may be indicative of a larger grain size, the subpixel mixing of unconsolidated grains with small amounts of consolidated material, or a crust on this surface, which would raise the thermal inertia relative to unconsolidated material of the same grain diameter. When the darker bed forms (B_1) and lighter toned material (B_3) are adjacent to one another, the darker bed forms cut the lighter-toned material bed forms, indicating an age relationship in which the lighter-toned material was in place before the darker bed forms were deposited. This relationship also suggests that the smaller, lighter bed forms are inactive material, and the darker bed forms have been more recently active [*Malin and Edgett*, 2001; *Wilson and Zimbelman*, 2004].

[54] Evidence for current aeolian activity on the Martian surface has been observed in the form of wind streak variability [e.g., *Sagan et al.*, 1972; *Arvidson*, 1974; *Veverka*, 1975; *Veverka et al.*, 1977; *Thomas and Veverka*, 1979; *Thomas et al.*, 1981], dust devil activity [e.g., *Thomas and Gierasch*, 1985; *Greeley et al.*, 2003; *Fisher et al.*, 2005], and the movement of sand-sized particles at the MER-Spirit landing site in Gusev Crater [e.g., *Arvidson et al.*, 2006; *Greeley et al.*, 2006]. In the absence of direct observations of dune migration in visible images [*Zimbelman*, 2000; *Edgett and Malin*, 2000; *Malin and Edgett*, 2001], it is difficult to determine with confidence the current activity of bed forms. However, there are other characteristics, such as lineations on dune slip faces and a lower albedo than the surrounding surfaces, that can help to establish the level of activity of Martian bed forms [*Edgett and Malin*, 2000]. The low TES albedo and DCI value indicate that there is little dust on the surface of these bed forms. The active migration of bed form features would prevent dust accumulation on their surface, and thus these dark bed forms currently may be saltating. Slip faces may be present on the low albedo dunes in MOC images, indicating particle movement, but they are at the limit of the image resolution and cannot be identified with confidence. In addition, the particle diameter inferred from thermal inertia data and the well-sorted nature of this material is consistent with active bed forms on Earth and is further evidence for current bed form activity in this area.

[55] This region consists of mesas, knobs, and ridges indicative of consolidated or lithified units that have been eroded (A). Three types of aeolian material are also present (B), and the different morphologic characteristics may represent variable degrees of bed form activity and different ages. The close proximity of actively saltating grains to the consolidated material suggests a feedback relationship between these units. The actively saltating grains may scour the consolidated unit, further eroding this material and exposing the observed layers. Unconsolidated sediment eroded from the consolidated material (A) may then be additional source material for either the dark or lighter-toned bed forms or the dark sand sheet. The erosive nature of the consolidated unit (A), and the thermal inertia, albedo, and DCI index of the unconsolidated material (B) all indicate that this region is dominated by aeolian activity.

5.3. Hebes Chasma Interior Layered Deposits

[56] Knowledge of the physical and chemical properties of layers on Mars is an important step toward understanding the evolution of Martian environments and climates. Hebes Chasma (centered at 284°E, ~1°N and ~310 km wide) is part of the Valles Marineris canyon system and contains a sequence of layered deposits that is ~5000 m in total thickness in its central plateau. Many possible emplacement environments for these layered materials, including effusive lava flows [e.g., *Komatsu et al.*, 1993; *McEwen et al.*, 1999], aeolian deposition [*Peterson*, 1981], lacustrine deposits [e.g., *Peterson*, 1981; *Nedell et al.*, 1987; *Komatsu et al.*, 1993; *Lucchitta et al.*, 1994; *Malin and Edgett*, 2000], subice volcanism [*Chapman and Tanaka*, 2001], and pyroclasic flows [e.g., *Peterson*, 1981; *Lucchitta et al.*, 1994; *Komatsu et al.*, 1993; *Hynek et al.*, 2003], have been suggested on the basis of morphologic characteristics

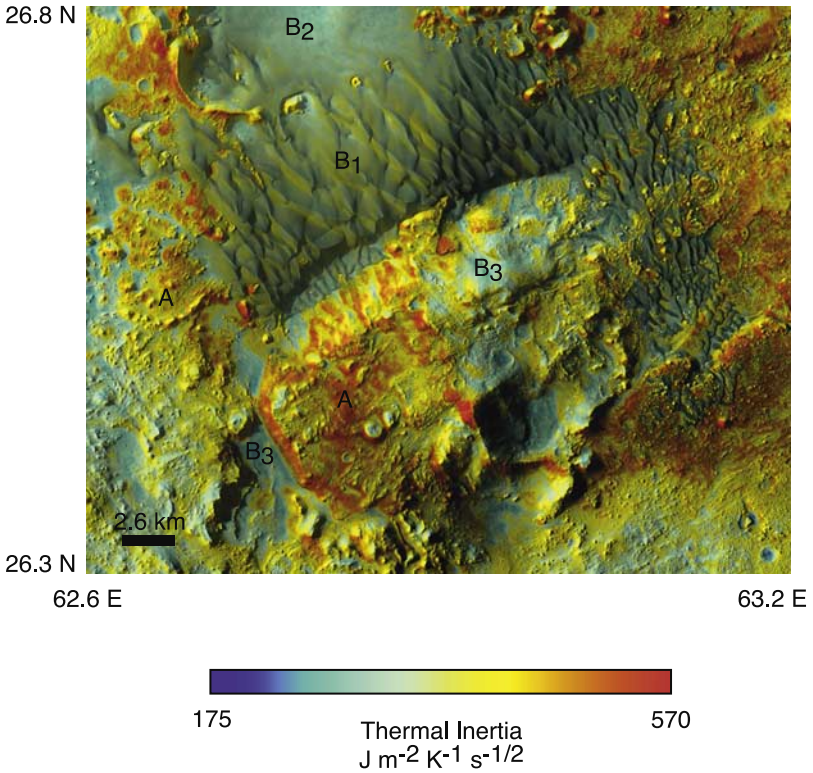

Figure 8. Sand in unnamed crater centered at 63°E, 26.5°N. THEMIS thermal inertia (100 m per pixel resolution) overlaid onto THEMIS visible image mosaic (18 m per pixel resolution) showing surfaces that have eroded into mesas, knobs, and ridges (A; yellow to red) and aeolian material (B; blue). The aeolian material has three morphologic expressions: a low albedo material that forms bed forms (B_1); a low albedo sheet that does not have bed forms at THEMIS visible resolutions (B_2); and material present between consolidated surfaces (B_3).

observed in visible images. The major layered units are resolvable by THEMIS infrared data, and sharp thermophysical boundaries correspond to changes in the morphologic characteristics observed in MOC and THEMIS visible images. Thus the thermal inertia is related to the underlying material and in most cases sediment mantles are not dominating the thermophysical properties; high-resolution thermal inertia data may help to constrain these depositional environments. Local slopes were included in the thermal inertia calculations, improving the accuracy of the thermal inertia estimates of these materials.

5.3.1. Unit Description

[57] The sequence presented below is a type example for the interior layered deposits exposed in the central plateau, consisting of five broad units (Figures 9 and 10). The presence of fine layers below THEMIS resolution is sug-

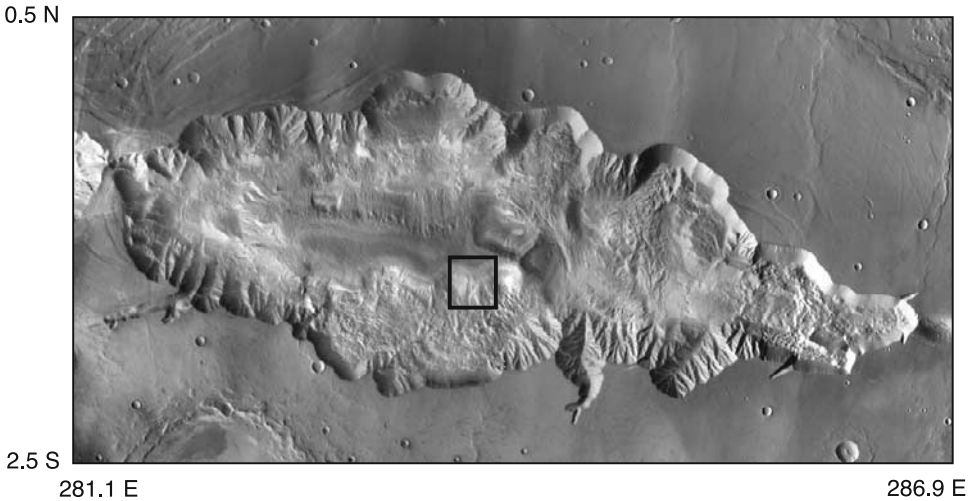

Figure 9. Hebes Chasma context. THEMIS daytime temperature mosaic of Hebes Chasma. The black box indicates the location of the THEMIS thermal inertia mosaic from Figure 10a.

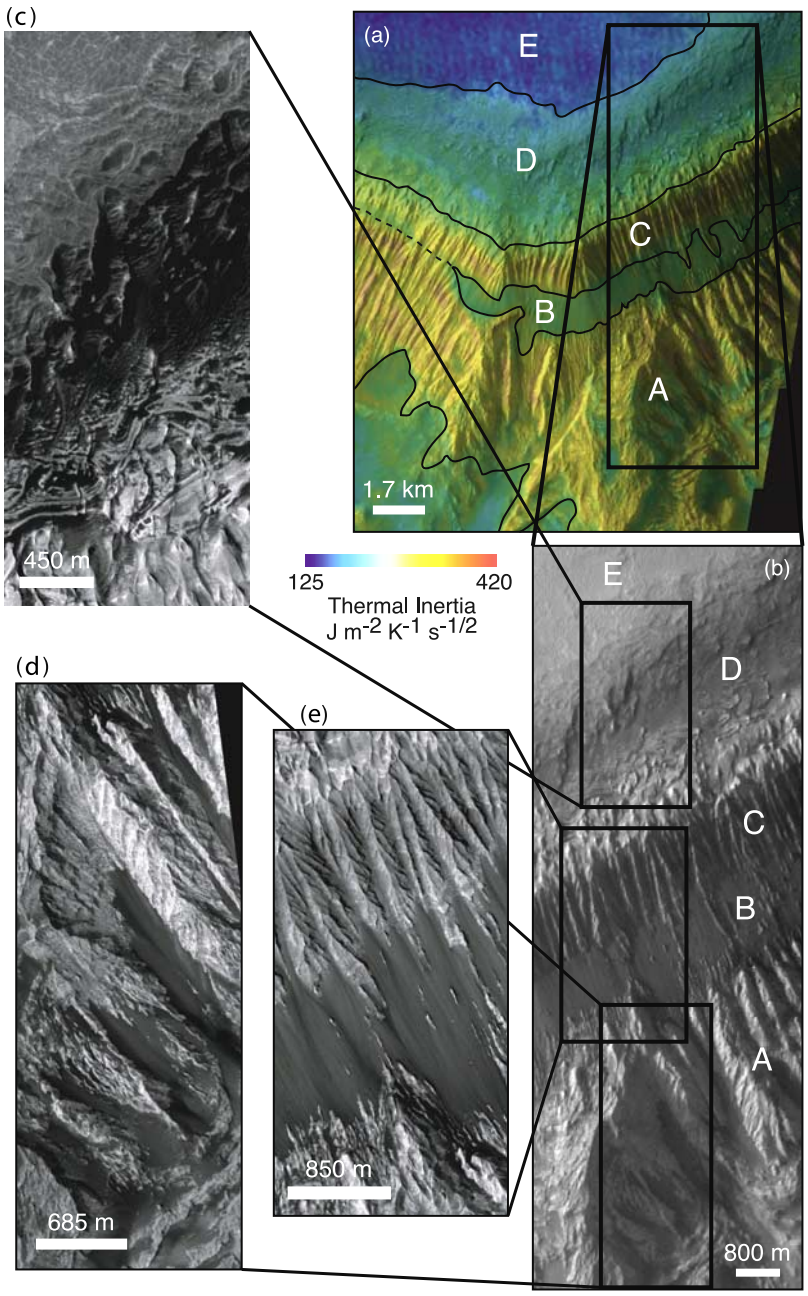

Figure 10. Hebes Chasma interior layered deposits. (a) THEMIS thermal inertia mosaic (100 m per pixel resolution) overlaid onto a THEMIS visible image V10052001 (18 m per pixel resolution) of Hebes Chasma, centered at 284 E, ~1 N. (b) THEMIS visible image V10052001. Capital letters represent layer units. (c, d, e) Enlargements from MOC Narrow Angle image M0900284, courtesy of Malin Space Science Systems (MSSS/NASA/JPL), of each layer unit.

gested in MOC images for all the units, implying multiple episodes of deposition within each unit, and possibly a repeated process. The layers appear to be continuous where exposed around the central plateau, however, landslide deposits obscure some areas. Beginning at the base of the central plateau, a ~2400-m-thick unit (A) has a thermal inertia of 290 to 420 (particle diameter of 780 μm (medium sand) and larger). This unit is eroding into a massive fluted morphology resembling yardangs that may be the precursor to spur-and-gully-type terrain [e.g., *Lucchitta*, 1979], and the presence of these erosional features on Unit A implies that it is indurated. Darker material is present within erosional grooves, has a thermal inertia of 270 to 290 (corresponding to a particle diameter of 575 to 780 μm; coarse sand), and is likely unconsolidated material derived from either Unit A or the above layers.

[58] Directly above Unit A is a ~600 m thick unit (B) that has a thermal inertia of 260 to 300 (particle diameter of 490 to 900 μm; medium to coarse sand), consistent with unconsolidated sand, suggesting that material has eroded

Table 5. Thermal Inertia of Materials[a]

	Density, ρ, kg m^{-3}	Conductivity, k, J s^{-1} °K^{-1} m^{-1}	Specific Heat, c, J kg^{-1} °K^{-1}	Thermal Inertia, J m^{-1} °K^{-1} s$^{-1/2}$
Sandstone (quartz)	2500	2.6 to 5.0	795	2270 to 3100
Basalt	2800	2.1	840	2215
Granite	2600	2.7 to 3.1	670	2180 to 2340
Rhyolite	2500	2.3	670	1960
Obsidian	2400	1.3	710	1465
Tuff (welded)	1800	1.2	840	1330

[a]Density, conductivity, and specific heat table values from *Kahle* [1980, Table 8.1].

from layers above and talus has preferentially accumulated in this region. Directly above Unit B, is a ~1000-m-thick unit (C) that has a thermal inertia of 275 to 385, which corresponds to a particle diameter of 620 μm (medium sand) and larger. This material is eroding into a fluted morphology [*Lucchitta*, 1979; *Peterson*, 1981; *Nedell et al.*, 1987; *Komatsu et al.*, 1993] in which the flutes are narrower than those observed in Unit A. The preservation of this fluted morphology indicates that this material is indurated, but the fine nature of the flutes suggests that it is not strongly resistant to erosion [*Komatsu et al.*, 1993] and is less competent than Unit A. The lower thermal inertia of Unit C relative to Unit A is also consistent with a less competent material than Unit A, as suggested by the morphology. Unit C may underlie Unit B in places because fluted material characteristic of Unit C is observed to poke through the unconsolidated material within Unit B.

[59] Above the fluted morphology of Unit C is a ~800-m-thick unit (D), which has a thermal inertia of 190 to 250 (particle diameter of 130 μm to 415 μm; fine to medium sand). The unit has a distinctive erosional pattern, forming a wavy, sinuous configuration suggestive of soft sediment deformation. Within Unit D, the albedo is dark toward the top of the plateau, and dark material is trapped in the scoured grooves toward the bottom of the unit. The peculiar erosional pattern further suggests that this unit is distinctive from those below it, and likely formed under different geologic conditions than the lower units. In the Melas Chasma interior layered deposits, material with a similar erosional pattern is observed at the top of the layered sequence with a sharp lower boundary and along the chasma floor, and is locally covered by dark sand dunes. These curved structures are interpreted to be due to lacustrian sedimentation within a local depression [*Quantin et al.*, 2005] or as block debris derived from the erosion of the interior layered deposits [*Weitz et al.*, 2003]. The erosional characteristics of Unit D are strikingly similar to the Melas Chasma material, and the possibility that Unit D was deposited in a fluvial environment cannot be ruled out. In addition, subice volcanic eruptions could form morphologic features similar to those found in Unit D [*Chapman and Tanaka*, 2001], and is another possible interpretation. The surface of the flat-lying central plateau (Unit E) has a thermal inertia ranging from 125 to 180, corresponding to ~100 diameter particles (very fine sand), and is some of the lowest thermal inertia material in Hebes Chasma. This material probably consists of a higher thermal inertia substrate and air-fall dust is currently accumulating on the flat surface, thereby lowering the apparent thermal inertia.

[60] Mafic materials have been previously identified in Valles Marineris layered deposits using Viking Orbiter color images [e.g., *Lucchitta*, 1987; *Geissler et al.*, 1990; *Komatsu et al.*, 1993] and Thermal Emission Spectrometer (TES) data [e.g., *Christensen et al.*, 1998]. The individual layers cannot be resolved, but the three-color Viking spectra of the Hebes Chasma deposits indicate a mafic composition that it is relatively unoxidized and presumed to be of volcanic origin [*Komatsu et al.*, 1993], and the TES spectra are consistent with basalt [*Christensen et al.*, 1998]. The thermal inertia of these layers is not high enough to be consistent with an effusive lava flow, but the mafic signature does indicate a volcanic origin. The lower thermal inertia suggests the secondary deposition of volcanic material as a weakly indurated sedimentary deposit or a volcanic ash deposit. This is in agreement with strength characteristics derived for interior layered deposits throughout Valles Marineris, which are consistent with softer sedimentary rocks and nonwelded tuffs [*Schultz*, 2002]. Unconsolidated sediment is present throughout these units and the subpixel mixing of lithified materials and unconsolidated sediment is likely lowering the apparent thermal inertia of these units. However, the morphologic characteristics observed in high-resolution MOC and THEMIS visible images indicate that the lithified material dominates the layered units. The strong correlation between the thermal inertia and the morphology of these layers is an additional indication that the lithified material, rather than the unconsolidated sediment, is dominating the thermophysical signature.

5.3.2. Interpretation

[61] The thermal inertia of the interior layered deposits in Hebes Chasma is too low to be consistent with an effusive lava flow. The highest thermal inertia of these deposits is 420, and unaltered basalt is expected to be ~2800 (Table 5). In addition, lava flows would likely be too well lithified to erode in the fluted pattern observed in Units A and C, and therefore is not a likely formation mechanism for these materials. A secondary emplacement of volcanic material in an aeolian environment would have a mafic signature and is likely to produce a lithology similar to sandstone found on Earth, which has a thermal inertia comparable to effusive basaltic lava (Table 5). The thermal inertia values are lower than expected for a sandstone-type material, but these layers could consist of a finer-grained precursor material or be weakly indurated. With the data provided, aeolian deposition of unconsolidated material cannot be ruled out as potential source material for the interior layered deposits.

[62] A lacustrian emplacement of the layers has been suggested for interior layered deposits observed in Hebes

Chasma and other localities [e.g., *Peterson*, 1981; *Nedell et al.*, 1987; *Komatsu et al.*, 1993; *Lucchitta et al.*, 1994; *Malin and Edgett*, 2000]. Horizontal layering is common for a lacustrian environment, and this type of layering is observed in Units A and C. Hebes Chasma does not have a well-developed fluvial system by which materials could be brought into the chasma. In addition, there is no observed outlet for removing water in the enclosed Hebes Chasma basin [e.g., *Chapman and Tanaka*, 2001]. The fluvial surface characteristics and outlet could have been obscured either by erosion or the deposition of additional material, but it seems unlikely that this obscuration would be pervasive throughout the chasma. Owing to the lack of fluvial features and outlet, a lacustrian environment is not a favored hypothesis for the formation of these deposits. The wavy, sinuous erosional pattern of Unit D is suggestive of soft sediment deformation and may be the result of plastic deformation of fluidized sediment rather than the deposition in a lacustrian environment.

[63] A volcanic ash deposit would have a lower thermal inertia than that of effusive lava, and could erode into the fluted pattern observed in Units A and C. Unit C appears less resistive to erosion and has a lower thermal inertia, implying a less indurated material than Unit A. Unit A could be a moderately welded tuff and Unit C may be a less consolidated volcanic ash deposit. This type of deposition is consistent with the observed mafic signature, derived rock strengths, the thermal inertia, and the erosional style of this deposit. The closest potential source is Tharsis Montes, and has previously been suggested as a source of volcanic ash [e.g., *Edgett*, 1997; *Hynek et al.*, 2003], and as a specific source for the interior layered deposits in Hebes Chasma [*Hynek et al.*, 2003].

[64] Aeolian deposition or a volcanic ash fall are the favored depositional mechanisms for the interior layered deposits in Hebes Chasma, as described in this work. The sharp thermophysical and morphologic boundaries between these layers strongly suggests a transition of depositional environments between these units, and a different depositional mechanism for each layer. Units A and C both erode in a fluted pattern, indicating that the material is weakly indurated yet resistive to erosion. Because of the similar morphologic features in these units, they likely formed by a similar process. The fluted morphology of Units A and C is consistent with a weakly indurated material or a fine-grained precursor material, and a weakly cemented sandstone or volcanic ash deposit is most likely to produce this type of morphologic pattern. Unit A is more lithified than Unit C as evidenced by the erosional morphology present and higher thermal inertia. Unit D exhibits a unique erosional pattern that is strikingly different from Units A or C, suggesting a significant change in the depositional environment and possibly the climate. This erosional pattern is suggestive of soft sediment deformation requiring some liquid medium. Our favored scenario for the deposition of the layered deposits in Hebes Chasma includes multiple episodes of volcanic ash or aeolian sediment deposition followed by lithification, resulting in the formation of Units A and C. Then the deposition of additional material in a fluidized medium occurred, but did not necessarily include a standing body of water.

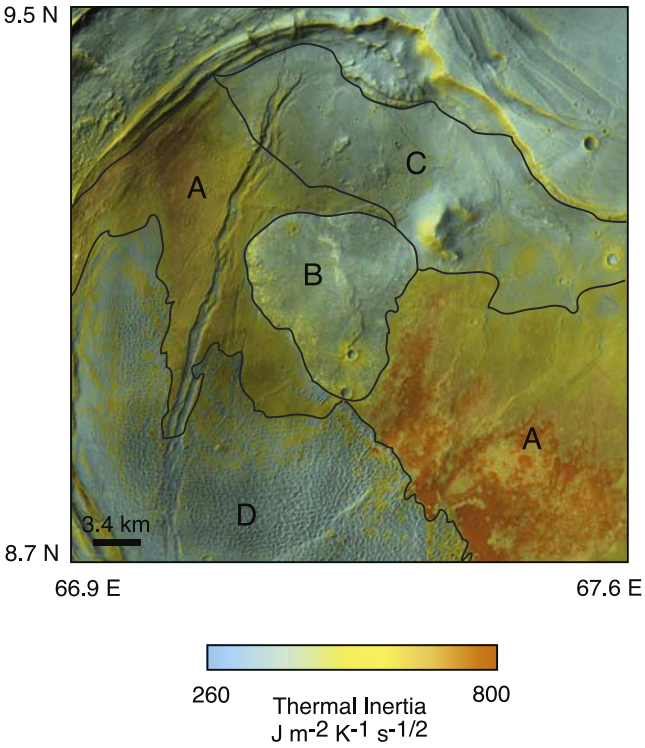

Figure 11. Nili Patera. THEMIS thermal inertia mosaic (100 m per pixel resolution) overlaid onto a THEMIS visible mosaic (18 m per pixel resolution) of Nili Patera, centered at 67°E, 9°N. Units A–D are discussed in the text.

5.4. Exposed Bedrock

[65] The identification of bedrock on Mars is important because it provides an opportunity to identify the chemical and physical characteristics of in situ material, and better constrain ancient environments or climates. The thermal inertia of a variety of common volcanic materials ranges from ~1300 to ~2800 (Table 5), and we use a value >1200 to define the thermal inertia of bedrock on Mars. High thermal inertia surfaces corresponding to exposed bedrock have been identified with THEMIS data, and these surfaces are found to range in size and to be exposed in a variety of geologic settings, such as crater interiors, channel walls, chaotic terrain, and the Martian plains [e.g., *Rogers et al.*, 2003; *Hynek*, 2004; *Hamilton and Christensen*, 2005; *Edwards et al.*, 2005]. Two focused studies of bedrock material identified using THEMIS data include Nili Patera [*Christensen et al.*, 2005] and Ares Vallis [*Rogers et al.*, 2005], and we compare our thermal model results with conclusions from those works.

5.4.1. Nili Patera

[66] One example of high thermal inertia material is found in Nili Patera (centered at 67°E, 9°N), which forms the northernmost caldera on the summit of a volcano in Syrtis Major. In this work, the Nili Patera region has been mapped (Figure 11) into four units: (A) high thermal inertia material; (B) volcanic cone; (C) lower thermal inertia material; and (D) aeolian material. The high thermal inertia material (Unit A) is found on both the western (410 to 610) and eastern (560 to 1180) portion of the caldera

floor, and was previously recognized by *Christensen et al.* [2003a] as very high thermal inertia material. Both regions of Unit A have a similar surface morphology and TES albedo (0.11 to 0.12), and were likely formed by similar processes. This material is interpreted to be a relatively fresh lava flow surface, consistent with *Christensen et al.* [2005]. The eastern exposure of this unit has a gradational thermal inertia that increases towards the west with the highest thermal inertias found closest to the aeolian sand. The highest thermal inertia material is consistent with bedrock (1180), and the lower thermal inertia (560 to 930) is interpreted to be bedrock with minor amounts of unconsolidated material that lower the observed thermal inertia, consistent with *Christensen et al.* [2003a, 2005]. It is likely that bed form movement across this surface has inhibited the accumulation of unconsolidated materials and air-fall dust and further exposed the high thermal inertia surface.

[67] The volcanic cone (Unit B) and the lower thermal inertia material north of the cone (Unit C) have a thermal inertia of 310 to 405. Unit B corresponds to a unique compositional unit in the caldera, characterized by a dacitic composition [*Christensen et al.*, 2005]. Although the thermal inertia of Unit B is lower than that of Unit A, it is also likely to be bedrock, because it exhibits a strong correlation between the thermophysical and morphologic boundaries. Superposition relationships suggest that Unit B postdates Unit A, but both units have similar crater densities indicating that they are similar in age [*Christensen et al.*, 2005]. The lower thermal inertia is likely caused by a thicker layer of locally derived loose material on the bedrock surface than Unit A, which may be several centimeters thick. Alternatively, Unit B may be a more porous material than Unit A, consistent with the interpretation of a dacite. Unit C has a similar morphology to Unit A, but a lower thermal inertia and is consistent with a bedrock surface overlaid by unconsolidated material. This layer of unconsolidated material is likely a few cm thick as it must be thick enough to lower the thermal inertia, but not completely mask the thermophysical properties of the underlying bedrock. The lower thermal inertia and the interpretation of a thicker layer of unconsolidated material present also suggests that the dunes did not recently (or ever) migrate across this surface.

[68] The aeolian material (Unit D) in Nili Patera is in the form of transverse dunes in the middle of the aeolian deposit and barchan dunes on the edges of the deposit. Both dune forms have a thermal inertia of 200 to 325, consistent with particle diameters of 160 to ~1 mm (fine to very coarse sand). The primary wind direction is from the northeast, as inferred from the location of the sand deposit in the southwestern portion of the caldera, the orientation of the barchan dunes, and the orientation of wind streaks to the east of the caldera. The sand likely migrated across the caldera floor, scouring loose sediment and leaving a surface of high thermal inertia.

5.4.2. Ares Vallis

[69] Another example of exposed bedrock detected by THEMIS is in Ares Vallis, centered at 340°E, 7°N. *Rogers et al.* [2005] identified three materials (described here as materials A–C) in the upper Ares Vallis region based on thermophysical, topographic, morphologic, and compositional evidence (Figure 12). The highest thermal inertia material (A) is an olivine-rich cliff-forming material that stands 10–250 m above the surrounding channel floor and typically has either a pitted or scoured appearance. *Rogers et al.* [2005] derived an average thermal inertia of 755 for this material using a thermal model provided by H. H. Kieffer, and interpreted this material to be in-place rock because of its sharp contacts, association with layered channel wall material, and little correlation with lower thermal inertia areas which are presumably unconsolidated aeolian material. Using the technique described here, the thermal inertia of this bedrock material is 950, higher than that derived by *Rogers et al.* [2005], and in agreement with the material interpretation. The intermediate thermal inertia material (B) primarily occurs in the channel floor, and is found in the lowest albedo regions. *Rogers et al.* [2005] derived an average thermal inertia for material B of 570 to 725, and interpreted it to be unconsolidated sand, a mixture of sand and coarser materials, or sand overlaying higher thermal inertia bedrock material. We calculate the thermal inertia to be 550 to 820, in good agreement with the values derived by *Rogers et al.* [2005]. They derived an average thermal inertia of 415 to 530 for layered wall materials (C); we calculate this material to have a thermal inertia of 440 to 560, in agreement with values derived by *Rogers et al.* [2005].

[70] The small differences between the thermal inertia values reported by *Rogers et al.* [2005] and those calculated here is primarily the result of a different visible/9-μm extinction opacity ratio used in each analysis. Another disparity is that we likely did not select exactly the same location as *Rogers et al.* [2005] when calculating the thermal inertia and may be incorporating slightly different material than was done in their study. However, the thermal inertia differences are not large enough to modify the interpretation of the surface characteristics or the understanding of geologic surfaces and processes.

6. Conclusions

[71] THEMIS infrared data have an improved spatial resolution (100 m per pixel) over previous data sets. Use of global thermal models to derive thermal inertia enables the quantification of surface physical characteristics to determine particle size information and identify surface exposures of bedrock. This new data set provides an improved understanding of geologic processes that have influenced the Martian surface. The overall accuracy of THEMIS thermal inertia is ~20%. The precision of the THEMIS thermal inertia values is 10–15%, and thus variations within a single THEMIS image closely represent differences in the physical properties of the surface.

[72] Despite differences between the TES and THEMIS data sets and the methods of deriving thermal inertia, the thermal inertia values are consistent with one another in terms of interpreting the physical surface properties and the surficial geology. THEMIS derived orbital thermal inertia values were compared to Mini-TES surface measurements with an average discrepancy of 10%, and this consistency lends confidence in the thermal inertia values derived from THEMIS.

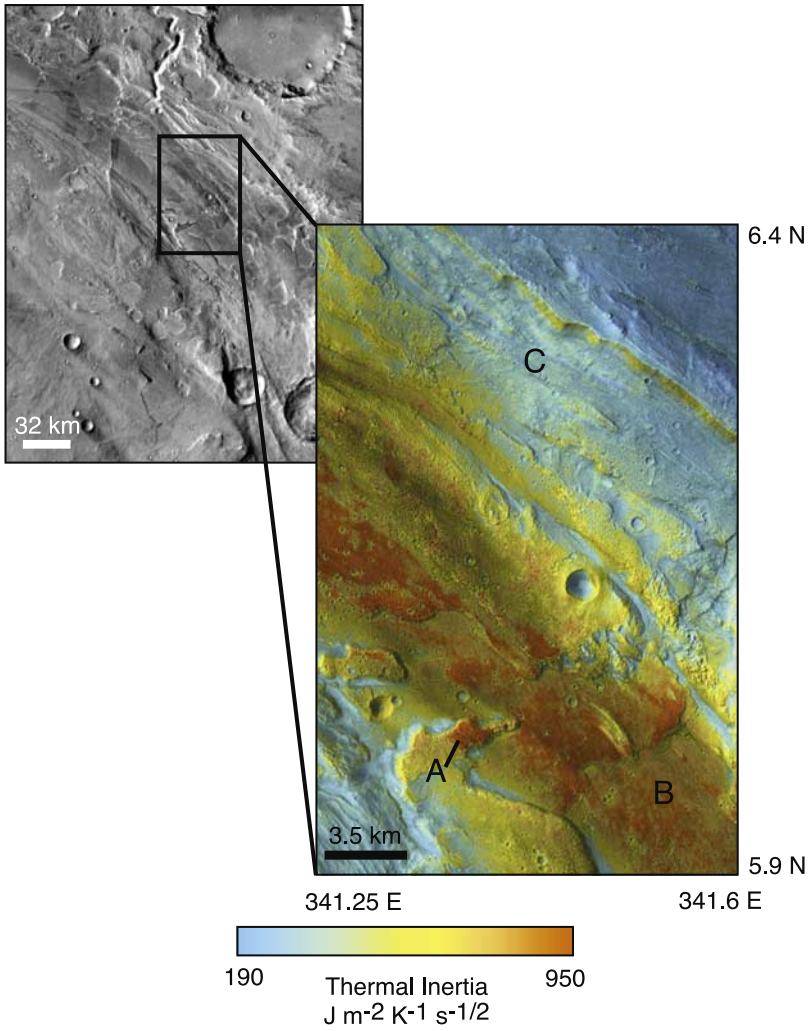

Figure 12. Ares Vallis. THEMIS thermal inertia mosaic (100 m per pixel resolution) overlaid onto a THEMIS visible image mosaic (18 m per pixel resolution) of the upper region of Ares Vallis, centered at 340°E, 7°N. Units A–C are discussed in the text.

[73] THEMIS thermal inertia enables an improved quantification of fine-scale surface detail observed in high-resolution THEMIS and MOC visible images, and also has near-global coverage at 100 m per pixel resolution. Dust surfaces, bed form material, interior layered deposits, and local outcrops of bedrock were studied to illustrate the improved understanding of surfaces provided by THEMIS thermal inertia data. In many cases, previously unknown stratigraphic relationships between thermal inertia and morphologic features were identified.

[74] 1. Although variable surface textures and individual lava flow fronts are observed in high-resolution visible images of Tharsis Montes, the thermal inertia at 100 m per pixel is uniform and indicates a layer of unconsolidated, likely air-fall dust that is a minimum of a few centimeters and up to 1–2 m thick. Individual features in visible images have no corresponding variation in the THEMIS thermal inertia images, indicating that the dust mantle is pervasive at THEMIS scales. Dust may currently be depositing in this region, but likely some process is allowing for the removal of that dust so that over time there is a net balance of dust accumulation and removal in this region.

[75] 2. Bed form material (centered at 63°E, 26.5°N) has a thermal inertia ranging from 230 to 340, indicating particle diameters expected for aeolian bed forms on Mars. The low albedo and well-sorted nature of this material is consistent with currently saltating material.

[76] 3. In Hebes Chasma, high resolution thermal inertia can distinguish variations in the physical nature of layers observed in the interior plateau. The thermal inertia of this material is too low to be consistent with bedrock or an effusive lava flow, and thus a secondary emplacement of volcanic material or a volcanic ash deposit is a more likely method of formation.

[77] 4. THEMIS thermal inertia enables the positive identification of exposed bedrock on the surface of Mars. Outcrops of bedrock have been identified in both Nili Patera and Ares Vallis. The thermal inertia boundaries correspond to distinct compositional and morphologic boundaries, suggesting that specific bedrock materials are exposed. The thermal inertia and morphology of adjacent terrain suggest that these bedrock surfaces are exposed by wind erosion and kept relatively free of dust and other unconsolidated material by aeolian processes.

[78] **Acknowledgments.** Ken Tanaka and James Zimbelman provided helpful reviews that improved this manuscript. Joshua Bandfield, Deanne Rogers, and Mike Wyatt read early drafts of this work, and Joshua Bandfield provided discussions regarding the calibration of the THEMIS instrument and the interaction between the atmosphere and the surface. Christopher Edwards helped construct the table used to create the final THEMIS global thermal inertia map. Noel Gorelick, Christopher Edwards, and Keith Nowicki developed and continue to improve the THEMIS mosaic software for both visible and infrared images, which enabled us to create the figures in this work. Ryan Luk created the first mosaic of the sand example. Saadat Anwar, Noel Gorelick, Dale Noss, and Randy Kaelber provided computer programming assistance. We also wish to thank THEMIS mission operations staff for collecting this data product, and acquiring images necessary to complete mosaics.

References

Arvidson, R. E. (1974), Wind-blown streaks, splotches, and associated craters on Mars: Statistical analysis of Mariner 9 photographs, *Icarus*, *21*, 12–27.

Arvidson, R. E., et al. (2006), Overview of the Spirit Mars Exploration Rover Mission to Gusev Crater: Landing site to Backstay Rock in the Columbia Hills, *J. Geophys. Res.*, *111*, E02S01, doi:10.1029/2005JE002499.

Bandfield, J. L. (2002), Global mineral distributions on Mars, *J. Geophys. Res.*, *107*(E6), 5042, doi:10.1029/2001JE001510.

Bandfield, J. L., D. Rogers, M. D. Smith, and P. R. Christensen (2004), Atmospheric correction and surface spectral unit mapping using Thermal Emission Imaging System data, *J. Geophys. Res.*, *109*, E10008, doi:10.1029/2004JE002289.

Bridges, N. T. (1994), Elevation-corrected thermal inertia and derived particle size on Mars and implications for the Tharsis Montes, *Geophys. Res. Lett.*, *21*(9), 785–788.

Chapman, M. G., and K. L. Tanaka (2001), Interior trough deposits on Mars: Subice volcanoes?, *J. Geophys. Res.*, *106*(E5), 10,087–10,100.

Christensen, P. R. (1982), Martian dust mantling and surface composition: Interpretation of thermophysical properties, *J. Geophys. Res.*, *87*(B12), 9985–9998.

Christensen, P. R. (1986), Regional dust deposits on Mars: Physical properties, age, and history, *J. Geophys. Res.*, *91*(B3), 3533–3545.

Christensen, P. R., and H. H. Kieffer (1979), Moderate resolution thermal mapping of Mars: The channel terrain around the Chryse Basin, *J. Geophys. Res.*, *84*(B14), 8233–8238.

Christensen, P. R., and H. J. Moore (1992), The Martian surface layer, in *Mars*, edited by H. H. Kieffer, et al., pp. 686–729, Univ. of Ariz. Press, Tucson.

Christensen, P. R., et al. (1992), Thermal Emission Spectrometer experiment: Mars Observer Mission, *J. Geophys. Res.*, *97*(E5), 7719–7734.

Christensen, P. R., et al. (1998), Results from the Mars Global Surveyor Thermal Emission Spectrometer, *Science*, *278*, 1692–1698.

Christensen, P. R., et al. (2001), Mars Global Surveyor Thermal Emission Spectrometer experiment: Investigation description and surface science results, *J. Geophys. Res.*, *106*(E10), 23,823–23,871.

Christensen, P. R., et al. (2003a), Morphology and composition of the surface of Mars: Mars Odyssey THEMIS results, *Science*, *300*, 2056–2061.

Christensen, P. R., et al. (2003b), Miniature Thermal Emission Spectrometer for the Mars Exploration Rovers, *J. Geophys. Res.*, *108*(E12), 8064, doi:10.1029/2003JE002117.

Christensen, P. R., et al. (2004), The Thermal Emission Imaging System (THEMIS) for the Mars 2001 Odyssey mission, *Space Sci. Rev.*, *110*, 85–130.

Christensen, P. R., et al. (2005), Evidence for magmatic evolution and diversity on Mars from infrared observations, *Nature*, *436*, doi:10.1038/nature03639.

Clancy, R. T., S. W. Lee, G. R. Gladstone, W. W. McMillan, and T. Rousch (1995), A new model for Mars atmospheric dust based upon analysis of ultraviolet through infrared observations from Mariner 9, Viking, and Phobos, *J. Geophys. Res.*, *100*(E3), 5251–5263.

Clancy, R. T., B. J. Sandor, M. J. Wolff, P. R. Christensen, M. D. Smith, J. C. Pearl, B. J. Conrath, and R. J. Wilson (2000), An intercomparison of ground-based millimeter, MGS TES, and Viking atmospheric temperature measurements: Seasonal and interannual variability of temperatures and dust loading in the global Mars atmosphere, *J. Geophys. Res.*, *105*(E4), 9553–9571.

Edgett, K. S. (1997), Aeolian dunes as evidence for explosive volcanism in the Tharsis Region of Mars, *Icarus*, *130*, 96–114.

Edgett, K. S., and M. C. Malin (2000), New views of Mars eolian activity, materials, and surface properties: Three vignettes from the Mars Global Surveyor Mars Orbiter Camera, *J. Geophys. Res.*, *105*(E1), 1623–1650.

Edwards, C. S., J. L. Bandfield, P. R. Christensen, and R. L. Fergason (2005), Global distribution of bedrock on Mars using THEMIS high resolution thermal inertia, *Eos Trans. AGU*, *86*(52), Fall Meet. Suppl., Abstract P21C-0158.

Fergason, R. L., P. R. Christensen, J. F. Bell III, M. P. Golombek, K. E. Herkenhoff, and H. H. Kieffer (2006), Physical properties of the Mars Exploration Rover landing sites as inferred from Mini-TES derived thermal inertia, *J. Geophys. Res.*, *111*, E02S21, doi:10.1029/2005JE002583.

Fisher, J. A., M. I. Richardson, C. E. Newman, M. A. Szwast, C. Graf, S. Basu, S. P. Ewald, A. D. Toigo, and R. J. Wilson (2005), A survey of Martian dust devil activity using Mars Global Surveyor Mars Orbiter Camera images, *J. Geophys. Res.*, *110*, E03004, doi:10.1029/2003JE002165.

Fountain, J. A., and E. A. West (1970), Thermal conductivity of particulate basalt as a function of density in simulated lunar and Martian environments, *J. Geophys. Res.*, *75*(20), 4063–4069.

Geissler, P. E., R. B. Singer, and B. K. Lucchitta (1990), Dark materials in Valles Marineris: Indications of the style of volcanism and magmatism on Mars, *J. Geophys. Res.*, *95*(B9), 14,399–14,413.

Golombek, M. P., et al. (2005), Assessment of Mars Exploration Rover landing site predictions, *Nature*, *436*, doi:10.1038/nature03600.

Greeley, R., R. Leach, B. White, J. Iversen, and J. Pollack (1980), Threshold windspeeds for sand on Mars: Wind tunnel simulations, *Geophys. Res. Lett.*, *7*(2), 121–124.

Greeley, R., M. R. Balme, J. D. Iversen, S. Metzger, R. Mickelson, J. Phoreman, and B. White (2003), Martian dust devils: Laboratory simulations of particle threshold, *J. Geophys. Res.*, *108*(E5), 5041, doi:10.1029/2002JE001987.

Greeley, R., et al. (2006), Gusev crater: Wind-related features and processes observed by the Mars Exploration Rover Spirit, *J. Geophys. Res.*, *111*, E02S09, doi:10.1029/2005JE002491.

Haberle, R. M., and B. M. Jakosky (1991), Atmospheric effects on the remote determination of thermal inertia on Mars, *Icarus*, *90*, 187–204.

Hamilton, V. E., and P. R. Christensen (2005), Evidence for extensive, olivine-rich bedrock on Mars, *Geology*, *33*(6), 433–436.

Hayashi, J. N., B. M. Jakosky, and R. M. Haberle (1995), Atmospheric effects on the mapping of Martian thermal inertia and thermally derived albedo, *J. Geophys. Res.*, *100*(E3), 5277–5284.

Hynek, B. M. (2004), Implications for hydrologic processes on Mars from extensive bedrock outcrops throughout Terra Meridiani, *Nature*, *431*, doi:10.1038/nature02902.

Hynek, B. M., R. J. Phillips, and R. E. Arvidson (2003), Explosive volcanism in the Tharsis region: Global evidence in the Martian geologic record, *J. Geophys. Res.*, *108*(E9), 5111, doi:10.1029/2003JE002062.

Jakosky, B. M. (1986), On the thermal properties of Martian fines, *Icarus*, *66*, 117–124.

Jakosky, B. M., M. T. Mellon, H. H. Kieffer, P. R. Christensen, E. S. Varnes, and S. W. Lee (2000), The thermal inertia of Mars from the Mars Global Surveyor Thermal Emission Spectrometer, *J. Geophys. Res.*, *105*(E4), 9643–9652.

Kahle, A. B. (1980), Surface thermal properties, in *Remote Sensing in Geology*, edited by B. S. Siegal, and A. R. Gillespie, pp. 257–273, John Wiley, Hoboken, N. J.

Kieffer, H. H., S. C. Chase Jr., E. Miner, G. Münch, and G. Neugebauer (1973), Preliminary report on infrared radiometric measurements from the Mariner 9 spacecraft, *J. Geophys. Res.*, *78*(20), 4291–4312.

Kieffer, H. H., T. Z. Martin, A. R. Peterfreund, B. M. Jakosky, E. D. Miner, and F. D. Palluconi (1977), Thermal and albedo mapping of Mars during the Viking primary mission, *J. Geophys. Res.*, *82*(28), 4249–4291.

Komatsu, G., P. E. Geissler, R. G. Strom, and R. B. Singer (1993), Stratigraphy and erosional landforms of layered deposits in Valles Marineris, Mars, *J. Geophys. Res.*, *98*(E6), 11,105–11,121.

Lucchitta, B. K. (1979), Landslides in Valles Marineris, Mars, *J. Geophys. Res.*, *84*(B14), 8097–8113.

Lucchitta, B. K. (1987), Recent mafic volcanism on Mars, *Science*, *235*, 565–567.

Lucchitta, B. K., N. K. Isbell, and A. Howington-Kraus (1994), Topography of Valles Marineris: Implications for erosional and structural history, *J. Geophys. Res.*, *99*(E2), 3783–3798.

Malin, M. C., and K. S. Edgett (2000), Sedimentary rocks of early Mars, *Science*, *290*, 1927–1937.

Malin, M. C., and K. S. Edgett (2001), Mars Global Surveyor Mars Orbiter Camera: Interplanetary cruise through primary mission, *J. Geophys. Res.*, *106*(E10), 23,429–23,570.

Malin, M. C., G. E. Danielson, A. P. Ingersoll, H. Masursky, J. Veverka, M. A. Ravine, and T. A. Soulanille (1992), Mars Observer Camera, *J. Geophys. Res.*, *97*(E5), 7699–7718.

McEwen, A. S., M. C. Malin, M. H. Carr, and W. K. Hartmann (1999), Voluminous volcanism on early Mars revealed in Valles Marineris, *Nature*, *397*, 584–586.

Mellon, M. T., B. M. Jakosky, H. H. Kieffer, and P. R. Christensen (2000), High- resolution thermal inertia mapping from the Mars Global Surveyor Thermal Emission Spectrometer, *Icarus*, *148*, 437–455.

Melosh, H. J. (1989), *Impact Cratering: A Geologic Process*, edited by H. Charnock, et al., 245 pp., Oxford Univ. Press, New York.

Nedell, S. S., S. W. Squyres, and D. W. Andersen (1987), Origin and evolution of the layered deposits in the Valles Marineris, Mars, *Icarus*, *70*, 409–441.

Neugebauer, G., G. Münch, H. Kieffer, S.C. Chase Jr., and E. Miner (1971), Mariner 1969 infrared radiometer results: Temperatures and thermal properties of the Martian surface, *Astron. J.*, *76*(8), 719–728.

Palluconi, F. D., and H. H. Kieffer (1981), Thermal inertia mapping of Mars from 60°S to 60°N, *Icarus*, *45*, 415–426.

Peterson, C. (1981), A secondary origin for the central plateau of Hebes Chasma, *Proc. Lunar Planet. Sci. Conf.*, *12B*, 1459–1471.

Pollack, J. B., D. S. Colburn, F. M. Flasar, R. Kahn, C. E. Carlston, and D. Pidek (1979), Properties and effects of dust particles suspended in the Martian atmosphere, *J. Geophys. Res.*, *84*(B6), 2929–2945.

Presley, M. A., and P. R. Christesen (1997a), Thermal conductivity measurements of particulate materials: 1. A review, *J. Geophys. Res.*, *102*(E3), 6535–6549.

Presley, M. A., and P. R. Christensen (1997b), Thermal conductivity measurements of particulate materials: 2. Results, *J. Geophys. Res.*, *102*(E3), 6551–6566.

Presley, M. A., and P. R. Christensen (1997c), The effect of bulk density and particle size sorting on the thermal conductivity of particulate materials under Martian atmospheric pressures, *J. Geophys. Res.*, *102*(E4), 9221–9229.

Putzig, N. E., M. T. Mellon, K. A. Kretke, and R. E. Arvidson (2005), Global thermal inertia and surface properties of Mars from the MGS mapping mission, *Icarus*, *173*, 325–341.

Quantin, C., P. Allemand, N. Mangold, G. Dromart, and C. Delacourt (2005), Fluvial and lacustrine activity on layered deposits in Melas Chasma, Valles Marineris, Mars, *J. Geophys. Res.*, *110*, E12S19, doi:10.1029/2005JE002440.

Rogers, A. D., J. L. Bandfield, and P. R. Christensen (2003), Global bedrock composition mapping on Mars using THEMIS and TES data, *Lunar Planet. Sci. [CD-ROM], XXXIV*, abstract 2082.

Rogers, A. D., P. R. Christensen, and J. L. Bandfield (2005), Compositional heterogeneity of the ancient Martian crust: Analysis of Ares Vallis bedrock with THEMIS and TES data, *J. Geophys. Res.*, *110*, E05010, doi:10.1029/2005JE002399.

Ruff, S. W., and P. R. Christensen (2002), Bright and dark regions on Mars: Particle size and mineralogical characteristics based on Thermal Emission Spectrometer data, *J. Geophys. Res.*, *107*(E12), 5127, doi:10.1029/2001JE001580.

Sagan, C., et al. (1972), Variable features on Mars: Preliminary Mariner 9 Television results, *Icarus*, *17*, 346–372.

Schultz, R. A. (2002), Stability of rock slopes in Valles Marineris, Mars, *Geophys. Res. Lett.*, *29*(19), 1932, doi:10.1029/2002GL015728.

Smith, D. E., and M. T. Zuber (1998), The relationship between MOLA Northern Hemisphere topography and the 6.1-mbar atmospheric pressure surface of Mars, *Geophys. Res. Lett.*, *25*(24), 4397–4400.

Smith, D., et al. (1999), The global topography of Mars and implications for surface evolution, *Science*, *284*, 1495–1503.

Smith, D. E., et al. (2001), Mars Orbiter Laser Altimeter: Experiment summary after the first year of global mapping of Mars, *J. Geophys. Res.*, *106*(E10), 23,689–23,722.

Smith, M. D., J. C. Pearl, B. J. Conrath, and P. R. Christensen (2000), Mars Global Surveyor Thermal Emission Spectrometer (TES) observations of dust opacity during aerobreaking and science phasing, *J. Geophys. Res.*, *105*(E4), 9539–9552.

Smith, M. D., J. C. Pearl, B. J. Conrath, and P. R. Christensen (2001), One Martian year of atmospheric observations by the Thermal Emission Spectrometer, *Geophys. Res. Lett.*, *28*(22), 4263–4266.

Thomas, P., and P. J. Gierasch (1985), Dust devils on Mars, *Science*, *230*, 175–177.

Thomas, P., and J. Veverka (1979), Seasonal and secular variation of wind streaks on Mars: An analysis of Mariner 9 and Viking data, *J. Geophys. Res.*, *84*(B14), 8131–8146.

Thomas, P., J. Veverka, S. Lee, and A. Bloom (1981), Classification of wind streaks on Mars, *Icarus*, *45*, 124–153.

Veverka, J. (1975), Variable features on Mars V: Evidence for crater streaks produced by wind erosion, *Icarus*, *25*, 595–601.

Veverka, J., P. Thomas, and R. Greeley (1977), A study of variable features on Mars during the Viking Primary Mission, *J. Geophys. Res.*, *82*(28), 4167–4187.

Wechsler, A. E., and P. E. Glaser (1965), Pressure effects on postulated lunar materials, *Icarus*, *4*, 335–352.

Wechsler, A. E., P. E. Glaser, and J. A. Fountain (1972), Thermal properties of granulated materials, from *Thermal Characteristics of the Moon*, *Prog. Astron. Aeronaut.,* vol. 28, edited by J. W. Lucas, pp. 215–241, MIT Press, Cambridge, Mass.

Weitz, C. M., T. J. Parker, M. H. Bulmer, F. S. Anderson, and J. A. Grant (2003), Geology of the Melas Chasma landing site for the Mars Exploration Rover mission, *J. Geophys. Res.*, *108*(E12), 8082, doi:10.1029/2002JE002022.

Wentworth, C. K. (1922), A scale of grade and class terms for clastic sediments, *J. Geol.*, *30*, 377–392.

Wilson, S. A., and J. R. Zimbelman (2004), Latitude-dependent nature and physical characteristics of transverse aeolian ridges on Mars, *J. Geophys. Res.*, *109*, E10003, doi:10.1029/2004JE002247.

Woodside, W., and J. H. Messmer (1961), Thermal conductivity of porous media: I. Unconsolidated sands, *J. Appl. Phys.*, *32*(9), 1688–1699.

Zimbelman, J. R. (2000), Non-active dunes in the Acheron Fossae region of Mars between the Viking and Mars Global Surveyor eras, *Geophys. Res. Lett.*, *27*(4), 1069–1072.

Zimbelman, J. R., and H. H. Kieffer (1979), Thermal mapping of the northern equatorial and temperate latitudes of Mars, *J. Geophys. Res.*, *84*(B14), 8239–8251.

Zimbelman, J. R., and L. A. Leshin (1987), A geologic evaluation of thermal properties for the Elysium and Aeolis Quadrangles of Mars, *J. Geophys. Res.*, *92*(B4), suppl., E588–E596

Zuber, M. T., D. E. Smith, S. C. Solomon, D. O. Muhleman, J. W. Head, J. B. Garvin, J. B. Abshire, and J. L. Bufton (1992), The Mars Observer Laser Altimeter investigation, *J. Geophys. Res.*, *97*(E5), 7781–7797.

P. R. Christensen and R. L. Fergason, School of Earth and Space Exploration, Mars Space Flight Facility, Arizona State University, Box 876305, Tempe, AZ 85287–6305, USA. (robin.fergason@asu.edu)

H. H. Kieffer, Celestial Reasonings, 2256 Christmas Tree Lane, Carson City, NV 89703, USA.